Mechanical strain focusing at topological defect sites in regenerating Hydra

Yonit Maroudas-Sacks[1*], S Suganthan[2], Liora Garion[1], Yael Ascoli-Abbina[1], Ariel Westfried[1], Noam Dori[1], Iris Pasvinter[1], Marko Popović[2,3,4,#] Kinneret Keren[1,5#]

[1] Department of Physics, Technion – Israel Institute of Technology, Haifa 32000, Israel

[2]Max-Planck Institute for Physics of Complex Systems, MPI-PKS, Nothnitzer Str. 38, Dresden, 01187, Germany.

[3]Cluster of Excellence, Physics of Life, Technische Universitat Dresden, Arnoldstrasse 18, Dresden, 01307, Germany.

[4]Center for Systems Biology, Pfotenhauerstrasse 108, Dresden, 01307, Germany.

[5] Network Biology Research Laboratories and Russell Berrie Nanotechnology Institute, Technion – Israel Institute of Technology, Haifa 32000, Israel

* current address:

Cluster of Excellence, Physics of Life, Technische Universitat Dresden, Arnoldstrasse 18, Dresden, 01307, Germany and Max Planck Institute of Molecular Cell Biology and Genetics, Pfotenhauerstrasse 108, Dresden, 01307, Germany.

[#] corresponding authors

Abstract

The formation of a new head during Hydra regeneration involves the establishment of a head organizer that functions as a signaling center and contains an aster-shaped topological defect in the organization of the supracellular actomyosin fibers. Here we show that the future head region in regenerating tissue fragments undergoes multiple instances of extensive stretching and rupture events from the onset of regeneration. These recurring localized tissue deformations arise due to transient contractions of the supracellular ectodermal actomyosin fibers that focus mechanical strain at defect sites. We further show that stabilization of aster-shaped defects is disrupted by perturbations of the Wnt signaling pathway. We propose a closed-loop feedback mechanism promoting head organizer formation, and develop a biophysical model of regenerating Hydra tissues that incorporates a morphogen source activated by mechanical strain and an alignment interaction directing fibers along morphogen gradients. We suggest that this positive feedback loop leads to mechanical strain focusing at defect sites, enhancing local morphogen production and promoting robust organizer formation.

INTRODUCTION

Morphogenesis requires elaborate coordination between multiple biochemical and biophysical processes to generate robust, functional outcomes. To achieve this, the system must employ feedback spanning all levels of organization that can relate the emerging patterns with the mechanisms driving their formation (Braun and Keren, 2018; Collinet and Lecuit, 2021). There is a growing appreciation for the role that mechanics plays in this process, and in particular the importance of mechanical feedback across scales in directing robust morphogenetic patterning (Dye et al., 2021; Hannezo and Heisenberg, 2019; Maroudas-Sacks and Keren, 2021). Cells can sense and respond to mechanical stimuli in diverse ways that can influence all aspects of their existence, from specific gene expression patterns to their structure and fate (Petridou et al., 2017). However, despite substantial progress in the field, the mechanisms by which such feedback operate and lead to the emergence of well-defined large-scale patterns remain largely elusive.

Hydra is a small fresh-water predatory animal that provides an excellent model system to study the feedback and integration between mechanics and other biophysical and biochemical processes in morphogenesis (Braun and Keren, 2018; Gierer, 2012). Hydra's structure is sufficiently complex to facilitate the exploration of fundamental features of multicellular animal development, yet it has a simple, radially-symmetric body plan and small size. Moreover, Hydra's capacity for full body regeneration and its short regeneration time facilitates the study of an entire morphogenetic process in a holistic manner (Braun and Keren, 2018).

The Hydra's body is composed of a bilayered epithelium that surrounds an internal, fluid-filled lumen. Due to the incompressibility of the fluid, the lumen acts as a hydrostatic skeleton that provides structural support to the tissue (Kier, 2012). The actomyosin cytoskeleton forms cortical networks and apical junctions in the bilayered Hydra epithelium, as well as actomyosin fibers, known as myonemes, that organize into coherent, parallel arrays that span the entire tissue (Aufschnaiter et al., 2017; Livshits et al., 2017). These arrays of supracellular contractile fibers run parallel to the body axis in the ectoderm, and perpendicular to the axis in the endoderm. All the epithelial cells in both layers are excitable, capable of generating Calcium-mediated action potentials that activate contraction of the supracellular actomyosin myonemes, as in muscles (Agam and Braun, 2023; Braun and Ori, 2019; Campbell et al., 1976; Szymanski and Yuste, 2019).

Hydra tissues undergo large deformations as part of their normal physiology as well as during regeneration (Bode and Bode, 1984; Wang et al., 2023a; Wang et al., 2019). The osmolarity difference between the fresh water environment and the lumen drives an inward osmotic flux (Ferenc et al., 2021; Futterer et al., 2003; Kucken et al., 2008), that inflates the lumen and increases the hydrostatic pressure gradient between the lumen and the external medium. This hydrostatic pressure together with internal actomyosin-driven force generation (Aufschnaiter et al., 2017; Wang et al., 2023a) are largely responsible for the large-scale tissue dynamics in Hydra, which facilitate the movements required for locomotion and catching prey in the mature animal (Szymanski and Yuste, 2019; Wang et al., 2023a), and drive the dynamic shape changes associated with morphogenesis in the regenerating tissue (Kucken et al., 2008; Livshits et al., 2017).

A crucial step in Hydra regeneration is the emergence of a new head organizer that functions as the main signaling center in the mature animal (Bode, 2012). The patterning of regenerating Hydra and the establishment of the new head organizer have been typically attributed to biochemical morphogens, primarily those associated with the Wnt signaling pathway and its autoregulatory dynamics (Hobmayer et al., 2000; Holstein, 2022; Nakamura et al., 2011). Indeed, local activation of Wnt can promote head organizer formation (Wang et al., 2020) and global Wnt activation results in a multi-headed phenotype (Broun et al., 2005; Ferenc et al., 2021). More recent work revealed that the Hippo-YAP pathway is also involved in axial patterning in Hydra, during budding (Broun et al., 2022) and regeneration from tissue segments and aggregates (Suzuki et al., 2023). Despite this progress, axial patterning in Hydra is still not well understood (Holstein, 2022). In particular, even though the significance of the head organizer was recognized over a century ago by Ethel Browne (Browne, 1909), the mechanisms involved in establishing a new head organizer and specifying its location remain obscure (Cazet et al., 2021; Gufler et al., 2018; Suzuki et al., 2023; Tursch et al., 2022).

Previously we found that the sites of topological defects in the nematic order (i.e., in the parallel alignment) of the supracellular ectodermal fibers emerge early (<24 hours from excision) in regenerating Hydra tissues, and coincide with the sites of formation of morphological features in the regenerating animal (Maroudas-Sacks et al., 2021). Specifically, early, aster-shaped +1 defects are located at the future head site of the regenerating tissue, and a pair of +½ defects come together at the site of the regenerating foot. Importantly, this asymmetry in the defect configuration is in accordance with a strong memory of body-axis polarity: the +1 defect forms within the originally head-facing region of the excised tissue (relative to the head of the parent Hydra), and the pair of +½ defects appear within the originally foot facing region (Shani-Zerbib et al., 2022).

Regenerating Hydra tissues undergo cycles of osmotic swelling and collapse (Ferenc et al., 2021; Futterer et al., 2003; Kucken et al., 2008). Previous experiments showed that increasing the osmolarity of the external medium leads to reduced rates of osmotic inflations in regenerating spheroids (Futterer et al., 2003; Kucken et al., 2008) and reduced activation of the Wnt signaling pathway (Ferenc et al., 2021). In particular, when the osmolarity of the external media is comparable to that of the lumen, Wnt expression falls off and head regeneration does not occur. While the mechanisms involved are unclear, the repression of the Wnt pathway and the failure to regenerate were attributed to the lack of tissue stretching under isotonic conditions (Ferenc et al., 2021). Note that this previous study assumed the tissue inflates uniformly, without considering the spatial organization of the contractile actomyosin fibers and the non-uniform stress they produce.

Here we study the dynamics of regenerating Hydra spheroids originating from rectangular tissue pieces at high spatiotemporal resolution using live imaging. We find that the tissue deformations during Hydra regeneration are highly non-homogeneous in both space and time, and that these deformations are correlated with the nematic organization of the ectodermal actomyosin fibers. In particular, we show that recurring transient tissue stretching is concentrated at sites that coincide with focal points of the actomyosin fiber pattern. Notably, we show that these foci, which can be identified in the folded spheroid *from the onset of the regeneration process*, coincide with the location where topological defects emerge and

eventually the regenerated head and foot form. The observed mechanical strain focusing is recapitulated by a biophysical model of Hydra tissue mechanics that considers transient activation of contraction in the ectodermal actomyosin fibers.

The fiber organization pattern in regenerating rectangular tissue segments is characterized by two foci, which appear similar initially. However, the region that will become the site of a +1 defect and later the head of the regenerated animal (in accordance with the memory of the original polarity (Shani-Zerbib et al., 2022)) experiences substantially larger stretching. This asymmetry in the deformation pattern continues following the formation of point nematic defects at these early focal sites, with large transient stretching localized at the +1 defect at the future head region and only smaller events occurring around the pair of +½ defects at the future foot site. We further find that rupture hole formation, that allows for rapid fluid release from the lumen, occurs exclusively at these actin foci throughout regeneration, primarily at the future head site. The ruptures are preceded by large stretching events that induce a transient increase in the in-plane stress at the rupture site.

The colocalization of focused tissue stretching, an aster-shaped defect in the actomyosin fiber organization, and the emergence of a biochemical signaling center associated with the regenerated head organizer, suggests a tight coupling between mechanics and biochemical signaling. We hypothesize that mechanical strain focusing, fiber organization and biochemical morphogens, could reinforce each other to direct robust formation of a new head organizer. We examine the relation between mechanics and biochemical morphogens, by disrupting the Wnt signaling pathway and characterizing the tissue dynamics and pattern of actomyosin fiber organization. Following inhibition of Wnt signaling using iCRT14, regeneration is hindered as previously observed (Cazet et al., 2021; Gufler et al., 2018), and the reorganization of the actomyosin fibers is completely disrupted. Furthermore, when tissue spheroids are subjected to elevated external osmolarity, which has recently been shown to suppress the Wnt signaling pathway over time and prevent regeneration (Ferenc et al., 2021), aster-shaped +1 defects are unstable. In this case, the actomyosin fibers do reorganize and reform an ordered nematic fiber array, but the spheroids develop an unusual defect configuration with two pairs of +½ defects at both ends and are unable to regenerate a new head.

Based on our experimental results, we propose a self-organization mechanism in which the actomyosin fiber organization and tissue mechanics are coupled to the dynamics of a biochemical morphogen via a closed-loop feedback mechanism. We hypothesize that this mechanochemical feedback loop underlies the robust formation and stabilization of the head organizer, and use model simulations to demonstrate the viability of this idea. As such, our work provides the basis for a putative mechanochemical framework for Hydra regeneration.

RESULTS

The actomyosin fibers form a reproducible pattern with two foci that become sites of topological defects

The dynamics of the organization of the ectodermal actomyosin fibers in regenerating Hydra are followed using live imaging of transgenic animals expressing Lifeact-GFP (Methods). Rectangular tissue segments cut from the body of mature Hydra fold and seal into closed hollow spheroids within a couple of hours (Bode and Bode, 1984; Javois et al., 1988; Livshits et al., 2017) (Fig. 1A,B). This process is highly stereotypical: opposite ends of the tissue stretch to meet, such that a section of the originally head-facing side of the excised tissue comes together with a section of the originally foot-facing side of the tissue (Shani-Zerbib et al., 2022). The excised tissue inherits an array of aligned actomyosin fibers, but during the folding process, some of the fibers disassemble, specifically along the edges of the excised tissue that stretch and meet to seal the spheroid (Livshits et al., 2017; Maroudas-Sacks et al., 2021). The resulting tissue spheroid contains a domain of well-ordered ectodermal fibers (corresponding to the more central part of the original excised tissue piece), and a region that lacks supracellular fiber organization (Figs. 1A,B, S1). The ordered domain of parallel ectodermal fibers spans roughly two-thirds of the tissue circumference in one direction. At either end of this ordered domain (along the fibers' direction), we find disordered 'caps' connected by a disordered 'bridge'. The two caps are mostly encircled by radially aligned fibers, whereas the connecting bridge is flanked on both sides by fibers aligned parallel to the domain boundary. This characteristic pattern allows us to identify two focal points of the actomyosin fiber organization as the centers of the disordered caps (Fig. 1A,B, S1). Overall, the disordered region has a total nematic charge of +2, defined by the fiber organization surrounding it (Fig. 1A).

The early stages of the regeneration process are characterized by an induction of order process, during which the partial array of inherited fibers guides the formation of aligned fibers throughout the tissue spheroid and point topological defects emerge (Maroudas-Sacks et al., 2021). We find that the location of the emerging point defects is highly stereotypical, forming at the center of the caps at the two foci of the actomyosin fiber organization (Figs. 1, S1). Using laser-induced uncaging of a caged dye (Abberior CAGE 552, see Methods) (Maroudas-Sacks et al., 2021), we selectively label groups of cells at the cap regions of folded spheroids and follow their location over time (Fig. 1C,D; Movie 1). The cap closer to the head-facing side of the excised tissue develops a +1 aster-shaped defect at the site of the future head of the regenerated animal, whereas in the other cap, a pair of +½ defects form at the future foot region. Meanwhile, the 'bridge' region between the two caps forms a complete, ordered array of fibers aligned parallel to the inherited fibers along its boundary. Typically, the bridge region becomes fully ordered before the point defects at either end are completely well-defined.

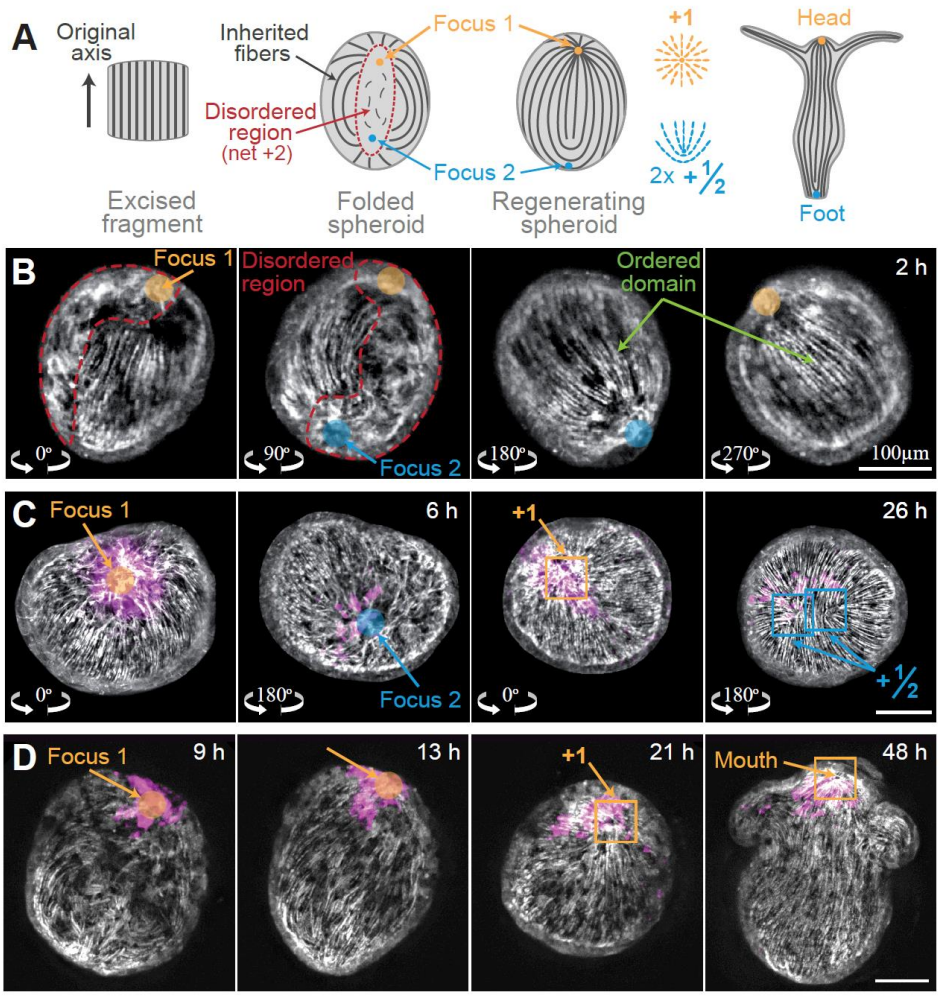

Figure 1. Foci of the actomyosin fiber organization. *(A) Schematic showing the fiber organization starting from an excised tissue fragment. The excised tissue folds into a closed hollow spheroid that contains an ordered fiber domain and a disordered region with a total topological charge of +2. The two actin foci within the initially disordered region develop into an aster-shaped +1 point defect at the future head site and a pair of +½ point defects at the future foot region. (B) Images of a regenerating tissue fragment 2 hours after excision. The spheroid was imaged from 4 directions, rotated 90º from each other, within a square FEP tube (Methods), and displays an actin fiber organization pattern with an ordered domain and a disordered region containing two disordered caps connected by a bridge. This characteristic pattern was observed in 46 out of 66 tissue spheroids similarly imaged 2-6 hours after excision. The remaining samples showed consistent behavior, but the pattern could not be clearly identified. (C) Images from a time-lapse movie of a regenerating Hydra acquired simultaneously from two opposite sides (Movie 1). The actin fiber organization (gray) is shown with an overlay of the photoactivated dye (magenta;* Abberior CAGE 552*). Left: the two actin foci within the disordered domain are visible from the two opposite sides at an early time-point. Right: images showing the same regions at a later time (as indicated by the tissue label marking small groups of cells), displaying the typical configuration of point defects that develop at the two foci. (D) Images from a time-lapse movie of a regenerating Hydra showing an actin fiber focus developing into an aster-shaped +1 defect, and then becoming the site of the mouth of the regenerated animal. The actin fiber organization (gray) is shown with*

an overlay of the photoactivated dye (magenta; Abberior CAGE 552*), identifying the cells in the vicinity of the actin foci at the onset of regeneration as the same cells that later become part of the head organizer at the tip of the head in the regenerated Hydra. All images are projected views of the basal surface of the ectoderm generated from 3D spinning-disk confocal images of live regenerating Hydra expressing Lifeact-GFP in the ectoderm.*

Mechanical strain focusing at foci of the actomyosin fiber organization

The tissue dynamics during regeneration are followed in conjunction with the actomyosin fiber organization at high spatiotemporal resolution using live 3D imaging. The Lifeact-GFP probe that labels the actomyosin fibers at the basal surface of the ectoderm, also binds to filamentous actin at the cell-cell junctions that line the cell boundaries at the apical ectodermal surface (Aufschnaiter et al., 2017). We developed an image processing pipeline to separate the fluorescent signal from the basal and apical sides of the ectoderm, allowing us to identify individual cells at the apical surface and characterize their shapes, while simultaneously measuring the basal supracellular actomyosin fiber organization (Methods). The regenerating Hydra tissue is extremely dynamic, with large-scale movements and continuous deformations. The most pronounced deformations are seen when the tissue experiences large-scale, coordinated contractions, that are reflected in extensive, yet transient, distortion of the tissue, primarily along the direction of the ectodermal actomyosin fibers (Fig. 2). During these events, we observe substantial stretching of cells at and around the foci of the actomyosin fiber organization (Fig. 2A), and at +1 defect sites following the induction of order at later stages of the regeneration process (Fig. 2B). Occasionally we observe 'doming', where the stretched tissue exhibits an abrupt change in tissue curvature between the core stretched region and the rest of the tissue (Fig. S2). The doming is suggestive of inhomogeneous or non-linear material properties in the tissue that produce excessive stretching near the core of the event and thus induce out-of-plane deformations (Latorre et al., 2018).

To quantify the frequency and localization of stretching events, we use spinning-disk confocal microscopy in a custom up-and-under setup, which enables simultaneous imaging of multiple samples from two opposite sides (Methods). We use movies with 2-2.5 minutes' time resolution, which is shorter than the typical event duration (7 ± 6 min, mean ± std, N=375 stretching events; Fig. 2F,I), and manually record all events that generate substantial tissue stretching (Fig. 2D-I). Larger stretching events, defined as incidents in which stretched cells reach about a 2-fold increase in apical cell area, are observed primarily at actomyosin foci within the disordered domain at earlier stage of the regeneration or later at sites of +1 defects (Fig. 2A,B,D; Movie 2). We concentrate on the first 24 hours of the regeneration process, during which a new organizer is likely established (Bode, 2012; Cazet et al., 2021; Gufler et al., 2018; Suzuki et al., 2023; Tursch et al., 2022), and observe recurring large stretching events primarily at the future head site at an approximately constant rate of ~1 event/hour (Fig. 2E). At later stages, as the regenerating tissue becomes elongated, it typically aligns parallel to the imaging plane, making it harder to visualize the defect regions. Nevertheless, the tissue deformations continue as the tissue regenerates and tentacles emerge, as well as afterwards in the mature animal, where contraction of the ectodermal fibers leads to stretching at the +1 defect region

and mouth opening (Carter et al., 2016). Notably, we never observe tissue stretching events in ordered regions, where the fibers are organized in a parallel array, and observe only smaller stretching events (with less than about 2-fold increase in apical cell area) at regions containing pairs of +½ defects (Fig. 2C,G).

The stretching events typically occur simultaneously at both actomyosin foci, but are noticeably asymmetric (Fig. S3). The future head region consistently exhibits larger amplitude events compared to the future foot region (Fig 2E,H). This is true even at earlier stages of the regeneration process, where both regions lack ordered fibers and we are unable to distinguish between them based only on the fiber organization. We have previously shown that the future head and future foot form in accordance with a strong memory of body-axis polarity (Javois et al., 1988; Shani-Zerbib et al., 2022). Thus, while the details of how body-axis polarity memory is encoded in the tissue remain unknown, our results indicate that there is a mechanical manifestation of this memory in the tissue deformations, which is apparent already at the early stages of the regeneration process (Fig. 2E,H).

The pattern of tissue deformations at the future foot and future head regions becomes more distinct as the fibers become organized and form the characteristic asymmetric defect configuration, with a +1 defect at the future head and a pair of +½ defects at the future foot site (Figs. 2B,C, S3). Events localized between pairs of +½ defects exhibit more moderate cell area stretching (Fig. 2C). In contrast, events at the future head region containing a +1 defect (Fig. 2B), remain radially symmetric around the defect and are similar in amplitude to earlier events (Fig. 2A). At these later stages, the difference between the pattern and extent of stretching at the future head region and future foot region, can be attributed to the different pattern of contractile fibers, and in particular the different configuration of point defects (+1 vs a pair of +½, respectively), at and around these two sites.

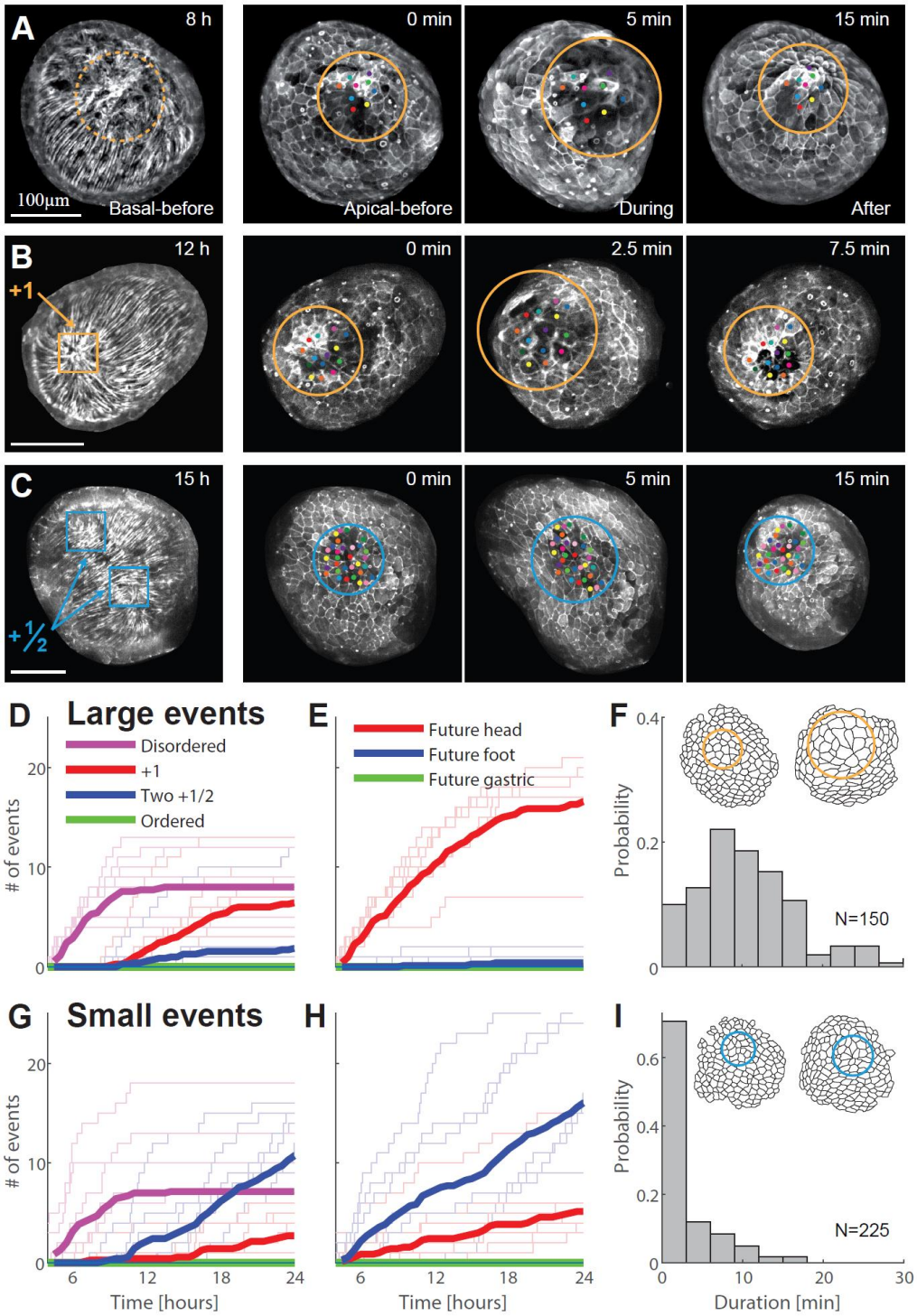

Figure 2. Tissue stretching events recur at the actin fiber organization foci. *(A-C) Images from time-lapse movies showing transient, local stretching events at foci of the actin fiber organization: (A) at the center of one of the caps in the early disordered domain; (B) at a well-defined +1 defect; and (C) at a pair of +½ defects. For each event, the left image depicts the actomyosin fibers at the basal surface of the ectoderm, and the right images show the apical surface throughout the event, with colored dots marking manually-tracked individual cells. All images are projected spinning-*

disk confocal images of regenerating tissues expressing Lifeact-GFP in the ectoderm. (D-I) Analysis of the distribution of larger (D-F) and smaller (G-I) stretching and rupture events. Widespread stretching events are manually identified and classified as large (more than ~2-fold cell area change or rupture) or small (less than ~2-fold cell area change; Methods). (D) Plot showing the cumulative number of large stretching and rupture events observed as a function of the fiber organization at the event site. The data is collected from 7 high-resolution movies of regenerating fragments imaged from both sides using an up-and-under microscopy setup (Methods). Stretching events are tracked during the first 24 hours of the regeneration process, starting 4 hours after excision (after the spheroids fold and seal). The thin lines depict results for individual movies, and the thick lines denote the mean over all samples. All samples regenerated, with an average regeneration time of 29±6 hours (mean±std). Local stretching events continue throughout the regeneration process and beyond, but become harder to visualize after >20 hours, since the regenerating animals typically elongate and orient themselves parallel to the imaging plane with the actin foci at the edges. (E) Plot showing the cumulative number of large stretching and rupture events for the same movies as in D, but broken down as a function of the morphological fate of the event site in the regenerated animal. (F) Histogram showing the duration of large stretching events occurring in the first 24 hours after excision. Inset: Schematic showing cell outlines during a large stretching event. (G-I) Plots as in D-F for small stretching events.

Characterization of the deformation pattern during stretching events

To quantify the pattern of ectodermal tissue deformations during stretching events in regenerating Hydra, we segment individual cells based on the Lifeact-GFP signal at the apical ectodermal surface that marks cell-cell junctions (Fig. 3; Methods). As in other epithelial tissues, segmentation of cells based on visualization of their boundaries provides a local measure of the tissue deformations calculated from cell geometries and their dynamics (e.g. (Blanchard et al., 2009; Etournay et al., 2015; Guirao et al., 2015; Hashimoto et al., 2015; Priya et al., 2020)). We correct for geometrical distortions in the projected view of the curved tissue surface, by calculating the cell shape and area for each cell from its boundary in the locally tangent plane (determined separately for each cell based on the average normal vectors of the curved surface in that cell; see Methods). Our ability to visualize and segment individual cells reveals dynamic and spatially inhomogeneous tissue strain patterns in regenerating Hydra, which could not be detected in previous studies that relied on lower-resolution imaging tools.

Given the observed radial pattern of tissue stretching around the foci of the actin fiber organization (Fig. 2), we use the actin focal point as a reference, and quantify the cellular deformations as a function of distance from this point (Fig. 3D-F). Tracking individual cells in regenerating Hydra is difficult due to the extensive deformations and highly dynamic nature of the tissue. However, the actin fiber pattern, which remains stable over the duration of stretching events (~several minutes; Fig. 2F,I), provides a useful relative frame of reference. Since absolute distances in the tissue strongly depend on the instantaneous tissue strain that is variable, we use graph distance (i.e. the degree of minimal neighbor separation between cells) to quantify the spatial pattern of deformations as a function of distance from the actin foci. This also allows us to group together cells at a particular graph distance from the defect, and measure how their mean area changes without needing to accurately track individual cells

(Methods). As the cells do not rearrange during stretching events, we determine the cell area strain by comparing the cell areas during the peak of a stretching event with the cell areas just before the event started. We measure area strain using the logarithmic strain, defined as the natural logarithm of the ratio of the cell areas during the peak event and just before it, since it is well-suited for large deformations.

We find that the area strain during stretching events is highest at the actin focal point at the future head region, located early on at the center of the cap region in the disordered domain and later at the site of the +1 defect (Fig. 3A,B). The area strain decays within a distance of ~3-5 cells from the foci (Fig. 3D,E). The amplitude of strain at the core varies between events, with an average logarithmic strain of ~ln(2), i.e. a two-fold increase in cell area (Fig. 3E). At the same time, cells away from the focus deform anisotropically, contracting along the direction of the ectodermal fibers (Fig. 3C). We quantify the degree of cell anisotropy using the cell shape tensor **Q** (Merkel et al., 2017) (see Methods). While the cell shapes at the core of the event remain essentially isotropic, we observe compressed cell shapes with enhanced anisotropy away from the actin foci (Fig. 3C,F). The deformation pattern at the future foot side that contains a pair of +½ defects is different, exhibiting only moderate local area stretching at the core (Fig. 3H-N). The cells in the regions between the pair of defects transiently contract along the fibers' direction, similar to what is observed in the ordered fiber arrays in the future gastric region.

The observed tissue stretching is not only localized in space, but also in time. Namely, the duration of stretching events is substantially shorter than the time period between the stretching events (Fig. 3D,K). Notably, the observed correlation between cell area stretching and the actomyosin fiber foci during stretching events (Fig. 3E,F,L,M), is not apparent during most of the regeneration process. In particular, the time-averaged changes in cell area strain around defect sites are substantially smaller than the changes observed during the peak of the stretching events, and well within the range of the typical variation in cell shape and area (Fig. 3G). Thus, while the area strain experienced by regenerating Hydra tissues during stretching events generates a clear mechanical signature at defect sites, the enhanced tissue deformations at these sites are transient and do not generate an appreciable effect upon time averaging. This suggests that if these tissue deformations provide relevant mechanical cues at the future head site, the response to these cues must be non-linear, accentuating the large yet transient strains encountered at defect sites.

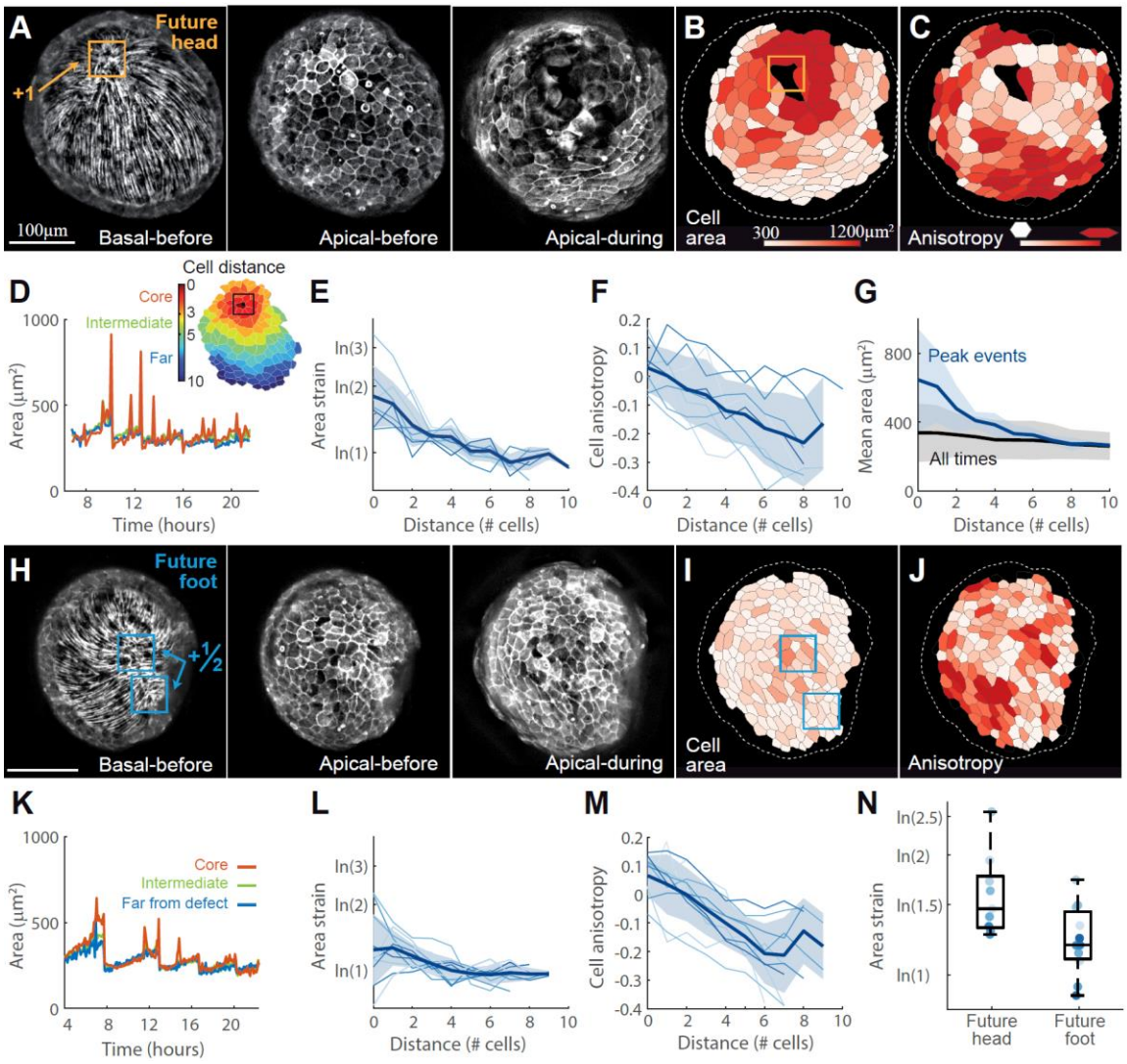

Figure 3. Characterization of mechanical strain focusing at foci of the actomyosin fiber organization. *(A) Images showing the fiber organization at the basal surface (left), and the cellular organization at the apical surface of a regenerating Hydra spheroid before (center) and at the peak (right) of a large stretching event localized at a +1 defect site at the future head region. (B,C) Cell segmentation maps at the peak of the stretching event shown in A, depicting cells labelled according to their area (B) or cell anisotropy (C; range: 0.1-0.65). (D) Plot of the mean cell area as a function of time, calculated from a fully-segmented time-lapse movie of a regenerating Hydra spheroid, imaged from the side of the future head site (Movie 3). The focal point is defined as the center of the cap region early on, or as the location of the +1 defect once formed. The observed tissue is divided into three regions: (i) core focus site, defined as a radius of 3 cells from the focal point (red), (ii) intermediate - cells at a distance of 4-5 cells from the focal point (green), and (iii) far from the focus - cells at a distance of 6 or more cells from the focal point (blue). The core focus region shows large, transient increases in cell area, which are not seen far from the defect. (E) The logarithmic area strain at the peak of individual stretching events at the future head site, as a function of distance from the focal point. The logarithmic strain is calculated as the log of the ratio of cell area at the peak of the event and before it, averaged for all cells at each distance. Distances*

are calculated as graph distances (degree of neighbor relation) between cells. Different shades of blue represent events at different time points (all from Movie 3; the color becomes darker with time). The bold line represents the mean over all events, and the shaded region represents the standard deviation. (F) Radial cell anisotropy as a function of distance from the defect, measured as the magnitude of the cell anisotropy tensor along the vector pointing towards the actin focal point (Methods). Events, mean and standard deviation are represented as in E. (G) The mean cell area as a function of distance from the focal point. The average cell area at every distance is calculated for each frame. The blue curve depicts the average over all frames at the peak of the stretching events, whereas the black curve shows the temporal average over the entire movie (mean±std). (H-M) Images and graphs showing the tissue dynamics in a regenerating Hydra spheroid at the future foot site, that include a stretching event localized around a pair of +½ defects (Movie 4) in analogy to the panels shown in A-F. The focal point here is defined as the center of the cap region early on, or as the mid-point between the location of the two +½ defects once formed. (N) Bar plot comparing the average of the log area strain at the core focus regions (defined as a radius of 3 cells from the focus point) at the future head and future foot sites for all events recorded in Movies 3 and 4. Individual events are characterized when the defect regions are facing the imaging plane, for a total of N=9 and N=11 events at the future head site and foot site, respectively. For each site the mean and standard deviation are shown together with the results from individual events (dots). All images are spinning-disk confocal projected images of spheroids expressing Lifeact-GFP in the ectoderm.

Rupture holes in regenerating Hydra spheroids form at foci of the actomyosin fiber organization

Regenerating Hydra spheroids exhibit cycles of swelling and collapse driven by osmotic influx of fluid into the lumen followed by tissue rupture and fluid release (Ferenc et al., 2021; Futterer et al., 2003; Kucken et al., 2008; Wang et al., 2019). The tissue ruptures typically involve disruption of both layers of the Hydra epithelium. This can be shown directly by imaging the ectoderm and endoderm simultaneously (Carter et al., 2016), as well as deduced indirectly from observations of the fluid efflux through rupture holes that is accompanied by a reduction in lumen volume (Ferenc et al., 2021; Futterer et al., 2003; Kucken et al., 2008; Maroudas-Sacks et al., 2021; Wang et al., 2019). Note that tissue ruptures could have various physiological implications including, e.g., release of internal pressure (Stokkermans et al., 2022), changes in the electric potential gradient across the tissue (Macklin and Josephson, 1971), and potential induction of a wound-healing response in the tissue (Tursch et al., 2022).

Our high-resolution imaging of tissue dynamics in regenerating Hydra allows us to directly visualize the formation of rupture holes and characterize their location and the associated tissue deformations. We find that osmotic inflations of the tissue spheroid involve gradual, essentially homogeneous increase in cell area throughout the ectodermal shell (Figs. 4A), likely due to a homogenous increase in the in-plane tissue stress induced by the influx of fluid into the lumen and the increase in hydrostatic pressure. However, rupture holes form exclusively at the foci of the actomyosin fiber organization, and their formation is preceded by inhomogeneous, local stretching of cells in the vicinity of the future hole site (Fig. 4; Movies 5,6). The rupture holes recur at the same locations, namely at one of the two actin foci sites, and never appear in regions with ordered fibers (Fig. 4A,F). This is true from the very first ruptures that occur in the

folded spheroid, contrary to what has been reported previously based on lower-resolution wide-field imaging (Wang et al., 2019). We further observe that the formation of rupture holes is biased toward the future head region (Fig. 4G), which we have found undergoes more extensive localized tissue stretching (Fig. 3N).

The tissue deformation pattern just before rupture, with mechanical strain focusing at the future rupture site and contraction of cells in the ordered regions far from this site (Fig. 4A), is analogous to the deformation pattern observed during stretching events (Figs. 2,3). As such, our observations indicate that the tissue ruptures are not the result of random, local failure following homogeneous osmotic inflations as previously thought (Ferenc et al., 2021; Kucken et al., 2008; Wang et al., 2019). Rather, the ruptures form when large-scale actomyosin fiber contractions occur in an osmotically-inflated tissue spheroid. In this case, the contractions further increase the isotropic pressure in the lumen (Stokkermans et al., 2022), and more importantly, generate an inhomogeneous in-plane stress component that is strongest at the foci of the fiber organization (see also modeling section below). The location of rupture hole formation is thus determined by the pattern of actomyosin fibers and the inhomogeneous in-plane stress that is concentrated at the actin foci during fiber contraction (Fig. 4F).

Rupture events typically involve disruptions of the epithelial bilayer along cell-cell contacts, generating fractures along cell boundaries (Fig. 4B), as observed in other tissues (Bonfanti et al., 2022). Immediately after their formation, the rupture holes can appear as elongated cracks along the junctions connecting adjacent cells (Fig. 4B). These cracks round up within a short time (<1 min) and acquire a smooth boundary with an enriched actomyosin ring, spanning multiple cells that lines the edge of the hole (Movie 5). The rupture holes typically reseal within ~10min (Fig. 4D). The formation of these rupture holes is reminiscent of the mechanism of mouth opening in adult Hydra, which also involves tearing of the epithelium along cell-cell junctions at a well-defined location that is a focal point of the ectodermal actomyosin fibers (Carter et al., 2016; Wang et al., 2019).

An interesting phenomenon that is observed in about half of the regenerating tissues (8 From 13 samples imaged from both sides) is the opening of extremely large rupture holes in the ectoderm, that can even reach the entire spheroid's circumference (Fig. 4C; Movie 6), and typically remain open for nearly an hour (Fig. 4E). Remarkably, despite the considerable deformation of the ectoderm during these events, the spheroids reseal and appear to recover their pre-rupture organization of fibers and cells and eventually regenerate successfully into functional animals. We suspect that these extremely large ruptures in the ectoderm may occur when the ectodermal layer partly detaches from the mesoglea due to the strong shear forces generated by the contraction of the ectodermal fibers. The large opening in the ectoderm in this scenario reflects transient sliding of the ectoderm relative to the endoderm, which subsequently recovers.

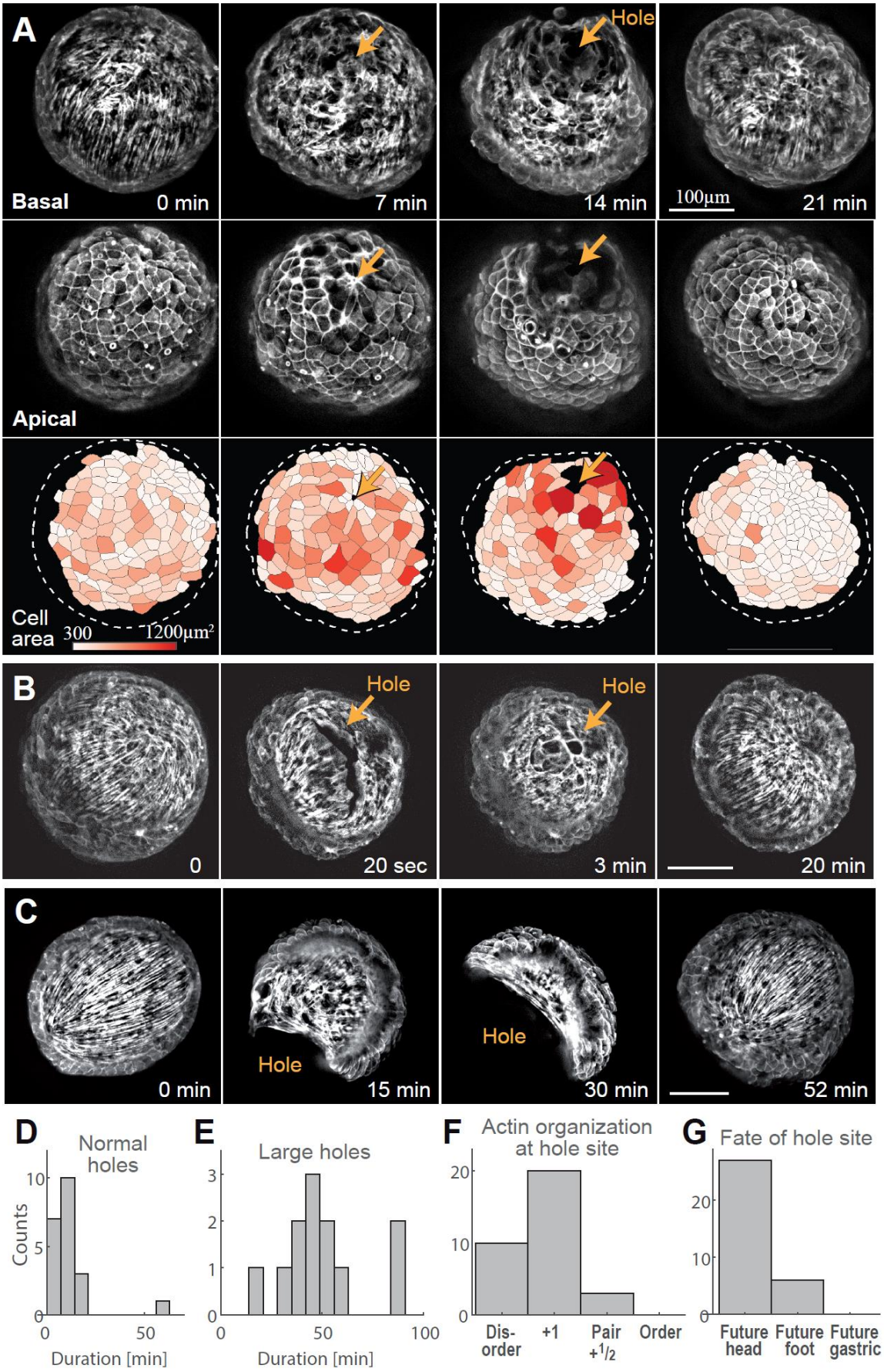
A
Hole
Basal
0 min
7 min
14 min
100µm
21 min
Apical
Cell area
300
1200µm²
B
Hole
Hole
0
20 sec
3 min
20 min
C
0 min
Hole
15 min
Hole
30 min
52 min
D
Normal holes
Counts
Duration [min]
E
Large holes
Duration [min]
F
Actin organization at hole site
Dis-order
+1
Pair +1/2
Order
G
Fate of hole site
Future head
Future foot
Future gastric

Figure 4. Rupture holes in regenerating tissue spheroids form at foci of the actin fiber organization. *(A-C) Examples of the opening and resealing of rupture holes at the future head site. The images (B,C and top row in A) show the basal ectodermal actomyosin fibers. In A, the middle row also shows the ectodermal apical surface, and the bottom row shows the segmented cells at the apical surface, color-coded according to their area. (A) Images from a time-lapse movie showing a rupture hole forming in a regenerating tissue fragment. The increase in cell areas following the osmotic inflation and the decrease in cell areas after the rupture event are roughly homogenous (left-most and right-most panels, respectively). In contrast, the stretching just before the rupture event is localized around the actin foci (third panel). (B) Images from a fast time-lapse movie showing a rupture that initiates as an elongated crack and rapidly becomes circular (Movie 5). (C) Images from a time-lapse movie showing the opening of an extremely large rupture hole (Movie 6). All images are projected spinning-disk confocal images of regenerating tissues expressing Lifeact-GFP in the ectoderm. (D) Histogram of the duration of small rupture holes (as in A,B). (E) Histogram of the duration of large rupture holes (as in C). (F) Bar plot showing the local actin organization at rupture hole sites. (G) Bar plot showing the future morphological outcome of rupture hole sites. The data in D-G is based on N=33 rupture holes identified during the first 24 hours after excision in 19 high resolution time-lapse movies of regenerating fragments.*

Theoretical modeling of mechanical strain focusing at foci of the actin fiber organization

The observed pattern of cell shape changes during the large stretching and rupture events can be understood intuitively by considering the organization of the ectodermal actomyosin fibers and assuming that the events correspond to global activation of contraction in these fibers. The local actomyosin fiber orientation dictates the anisotropy of the stress generation during their contraction. Upon global activation, the aster-shaped +1 defect regions will focus stress (and hence strain) at the defect site, due to the contraction of the surrounding radially-oriented fibers. Similar stress focusing is expected at the early foci of the actin fiber organization at the center of the cap region, which is encircled by radially-oriented fibers from nearly all directions (apart from the disordered bridge). The fiber organization in the vicinity of pairs of +½ defects is expected to be less efficient at focusing stress, due to the partially parallel fiber organization between the +½ defects, and no strain focusing is expected in ordered regions with a parallel array of fibers.

We assume that the ectodermal muscle fibers are the primary source of force generation during the large stretching events, and that the Hydra tissue is elastic (Perros et al., 2023). While the thinner, perpendicularly-oriented endodermal fibers also generate forces, we neglect their contribution to the tissue deformations during rapid stretching events. This assumption is justified by our observations that the tissue contracts primarily along the direction of the ectodermal fibers during these events (Fig. 3F,M). This is also consistent with recent studies of the behavior of mature Hydra that similarly show that the ectodermal fibers are dominant during large deformations (Wang et al., 2023a).

To corroborate our intuitive understanding of mechanical strain focusing during stretching events, we developed a biophysical model of Hydra tissue mechanics. In our model we describe

the regenerating Hydra as a deformable shell that encapsulates a fluid-filled lumen and contains an embedded nematic field describing the orientation of the actomyosin fibers. The deformable shell is realized as a collection of cells specified by the positions of their vertices. As such our model is a generalization of a 2D vertex model (Farhadifar et al., 2007; Honda and Eguchi, 1980) to curved closed surfaces. The mechanics of the model tissue is described by an energy function *E*, that accounts for cell area elasticity, cell-cell adhesion, and cell perimeter elasticity (Fig. 5A; further details in the Supplementary Information), as in standard vertex models (reviewed in (Alt et al., 2017; Fletcher et al., 2013)). The fluid-filled lumen imposes a constraint on the dynamics, namely, shape changes of the tissue have to conserve the lumen volume (Fig. 5A). Furthermore, since we do not explicitly model the tissue thickness, we include a bending energy term that penalizes tissue curvature. We describe the embedded nematic field associated with the actomyosin fibers, by assigning a two-dimensional nematic tensor to each cell in the cell-tangent plane. Finally, to emulate stresses generated by fiber contraction, we introduce active stresses in each cell, oriented along the nematic field, with a tunable magnitude ζ (Fig. 5A) (Comelles et al., 2021). The parameters of the model are chosen to reproduce the observed elastic behavior of the regenerating Hydra tissue and the magnitude of deformations observed experimentally (Supplementary Information).

We use this model to simulate individual tissue stretching events and quantitatively describe the induced strain patterns (Fig. 5, Movies 7,8). Starting from an initially relaxed state we emulate global contraction activation by introducing a pulse of active stress with magnitude ζ_M , which is selected to match the experimentally observed area strain magnitude (Fig. S4; Supplementary Information), and duration ΔT_ζ. Since the time scale for stretching events (minutes; Fig 2F,I) is shorter than the time scale for rearrangement of the actomyosin fibers (several hours (Maroudas-Sacks et al., 2021)), we assume that the nematic field describing the fiber orientation does not evolve during these events (apart from being conveyed by the cells as the tissue deforms). We consider two particular configurations of the nematic field that recapitulate the experimentally observed fiber patterns during early and later stretching events, respectively. For early stretching events, we consider a spheroid with a large disordered domain of net charge +2 surrounded by a fully ordered region (Fig. 5B). For later events, following the induction of order, we consider a spheroid with fully-ordered fibers except for a +1 defect on one end and a pair of +½ defects at the opposite end (Fig. 5C).

Simulating transient activation of contraction with a time-dependent active stress aligned with the nematic field, recapitulates the deformation patterns observed experimentally, with cell stretching concentrated at the two actin foci, and compression of cells along the direction of the fibers in the ordered regions between the foci (Fig. 5B-D, Movies 7,8). Since the fiber organization at early stages of the regeneration is similar around the two foci, the simulated mechanical strain focusing has a similar magnitude in both foci (Fig. 5E). This differs from the polar strain pattern observed in real tissues, which exhibits larger stretching amplitude in the future head region already at the onset of the regeneration process (Fig. 3). At later stages of the regeneration, when the nematic pattern becomes asymmetric, with a +1 defect at the future head region and a pair of +1/2 defects at the future foot region, the model accounts for the asymmetric deformation pattern observed experimentally with more pronounced stretching at the +1 defect site (Fig. 5C,F, Movie 8). The opposite end of the spheroid that has a pair of +½

defects displays a smaller magnitude of local stretching (Fig. 5D). Overall, these results demonstrate that considering regenerating Hydra tissue spheroids as elastic shells with an incompressible internal cavity, that undergo global activation of the nematically-aligned contractile fibers, is sufficient to account for the deformation patterns and overall tissue shape changes during stretching events.

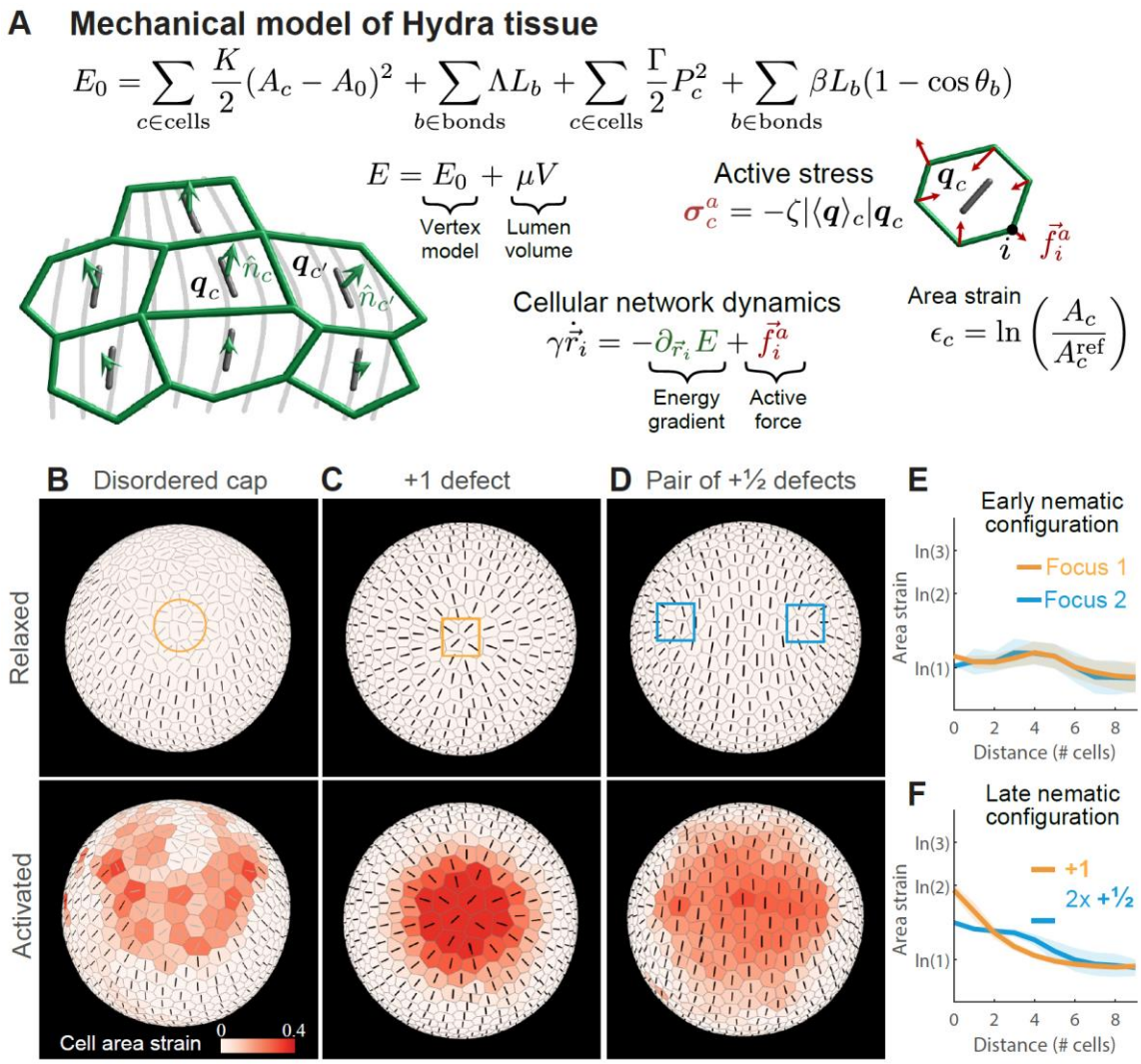

Figure 5. Model of Hydra tissue mechanics recapitulates strain focusing during stretching events. *(A) The equations describing the mechanical model of Hydra tissue. The Hydra tissue is described as a deformable elastic shell of cells using a generalization of the vertex model. The geometry of the cellular network is specified by the positions of cell vertices ($\vec{r}_i$) and its dynamics are driven by gradients of the vertex model energy function E and active stresses generated by the embedded nematic field $\boldsymbol{q}_c$. Motion of the cellular network is constrained by the lumen volume V through a Lagrange multiplier (μ). In our model equations, A_c and A_0 are the cell areas and preferred cell area, K is the area elastic modulus, Λ and L_b are the bond tension and bond length, Γ and P_c are the perimeter elastic modulus and cell perimeter, β is the cell-cell bending modulus and θ_b is the angle between normal vectors of neighboring cells that share the bond b. For further details, see Methods and Supplementary Information. (B) Mechanical strain focusing*

at one of the cap regions in a spheroid with a large disordered domain of net charge +2 that is surrounded by a fully ordered region, emulating the actomyosin fiber organization in regenerating fragments at early stages of the regeneration process. (C,D) Mechanical strain focusing at the two defect regions of a spheroid with an ordered nematic array, emulating the actomyosin fiber organization in regenerating fragments at later stages of the regeneration process. The strain patterns around the +1 defect on one side (C) and around the pair of +½ defects at the opposite end (D) are shown. In (B-D), the top panels depict the relaxed configurations before the event, and the bottom panels show the same regions during the peak of the stretching events. The cells are color-coded according to the area strain relative to the relaxed configuration and the orientation of the embedded nematic in each cell is depicted. (E,F) Plots of the simulated cell area strain during the peak of a stretching event as a function of distance in cells from the focus region. The cell area strain is defined as $\epsilon_c = ln(A_c/A_c^{ref})$, *where* A_c *is the cell area at the peak of the event and* A_c^{ref} *is the initial cell area at t=0. (E) Results from simulations of regenerating fragments at early stages of the regeneration process, showing stretching around the two foci in the cap regions, within the large disordered domain of net charge +2. (F) Results from simulations of regenerating fragments at later stages of the regeneration process, showing stretching around the +1 defect and the pair of +½ defects. The mechanical strain focusing is more prominent at the +1 defect due to the structure of the contractile fibers around this region.*

Inhibition of the Wnt pathway disrupts the formation of aster-shaped +1 defects

The coincidence of the +1 defect in the actin fiber orientation with the signaling center at the head organizer in mature Hydra (Fig. 6A), suggests an intimate coupling between mechanics and biochemical signaling. To explore the interplay between biochemical morphogens and tissue mechanics during regeneration and relate this to head organizer formation, it is useful to perturb the Wnt signaling pathway, which is considered to be the main activator associated with organizer formation, and characterize the influence on actin fiber organization, tissue dynamics and regeneration outcome.

Previous work has shown that local upregulation of Wnt leads to rearrangements of the ectodermal actomyosin fibers toward regions with high Wnt and the formation of aster-shaped +1 defects. This is true during budding, where the expression of Wnt at the tip of the emerging bud is accompanied by reorganization of the actin fibers and defect formation (Aufschnaiter et al., 2017). Similarly grafting of an excised organizer or a piece of tissue overexpressing Wnt onto a host tissue leads to reorganization of the actomyosin fibers toward the local Wnt peak (Wang et al., 2020). Furthermore, work in regenerating aggregates showed that clusters of 5-15 cells from head-regenerating tips develop into a head organizer in the regenerating aggregate and induce the formation of a hypostome with an aster-shaped defect (Technau et al., 2000).

To investigate the influence of down-regulation of Wnt on actin fiber organization and tissue mechanics we use iCRT14, which is a known inhibitor of β-Catenin-TCF interaction that has been shown to suppress the Wnt signaling pathway and inhibit regeneration of bisected Hydra (Cazet et al., 2021; Gufler et al., 2018). We follow the dynamics of excised tissue fragments subject to

iCRT14 treatment, and examine its effect on actin fiber organization and tissue mechanics. We pretreat the parent animal with 5µM iCRT14 for 2 hours prior to excision (Cazet et al., 2021), and subsequently maintain the excised tissues in the same concentration of iCRT14 (Methods). We find that excised fragments fold and seal as untreated samples, with a similar pattern of partial inherited parallel actin fibers and a large disordered region in the folded tissue spheroid (Fig. 6B, top). However, unlike control samples, the reorganization of the actin fibers is disrupted in treated fragments (Fig. 6B, bottom, Movie 9). While the inherited actomyosin fibers in the ordered region remain stable, there is no induction of order in the disordered region, so the fiber pattern remains essentially in its initial configuration with an inherited ordered region and a large disordered domain. Notably, under these conditions, aster-shaped point defects fail to form and the tissue fragments do not regenerate.

Recent experiments by Ferenc *et al.* (Ferenc et al., 2021) showed that placing regenerating Hydra spheroids in elevated osmolarity, among various possible effects, also leads to suppression of the Wnt signaling pathway. These experiments corroborated previous findings, showing that when regenerating tissue fragments are placed in media that is isotonic with their lumen (~70 mOsm), osmotic inflations cease (Kucken et al., 2008). They further showed that under these isotonic conditions, Wnt is initially up-regulated in response to the wound, but its expression is not sustained and subsequently declines, and the excised tissues fail to regenerate. Here we follow the tissue deformation and actin fiber dynamics in tissue fragments subject to elevated osmolarity. Tissue fragments are excised and allowed to seal in normal media for 3-4 hours, and subsequently placed in Hydra medium supplemented with 70mM sucrose. Initially, the folded spheroids have an ordered region and a disordered domain containing two foci (Fig. 6E, left), which rapidly organizes into an ordered nematic array of fibers (Movie 10). As in untreated samples, the establishment of an array of parallel fibers in the initially disordered domain, leads to the formation of point defects. However, under isotonic conditions, the spheroids develop an unusual defect configuration with two pairs of +½ defects, rather than the characteristic defect configuration with a +1 defect at the future head site and a pair of +½ defects at the future foot site (Maroudas-Sacks et al., 2021) (Fig. 6C,D).

We find that while the tissue still undergoes stretching events with mechanical strain focusing at the actin foci, these are diminished in comparison to control samples (Fig. S5; Movie 10). In particular, we observe fewer incidents of rupture hole formation under isotonic conditions and large stretching events are not observed in the four +½ defect configuration that develops. Interestingly, even though the tissues fail to regenerate, they still elongate along the direction of the fibers, such that the two pairs of +½ defects localize at either end of the cylindrical tissue, rotated 90° from each other (Fig. 6E, Movie 10). The stable defect configuration under isotonic conditions is noticeably different from the characteristic defect pattern in untreated samples, which develop a stable +1 defect at the future head site. Notably, while we occasionally observe the transient formation of an aster-shaped +1 defect in some samples under isotonic conditions, we find that these defects are unstable and dissolve into a pair of +½ defects (Fig. 6E; Movie 10). Overall, these results highlight the inherent coupling between actin fiber organization and Wnt signaling dynamics, and demonstrate that the formation of aster-shaped +1 defects can be disrupted when Wnt expression is perturbed.

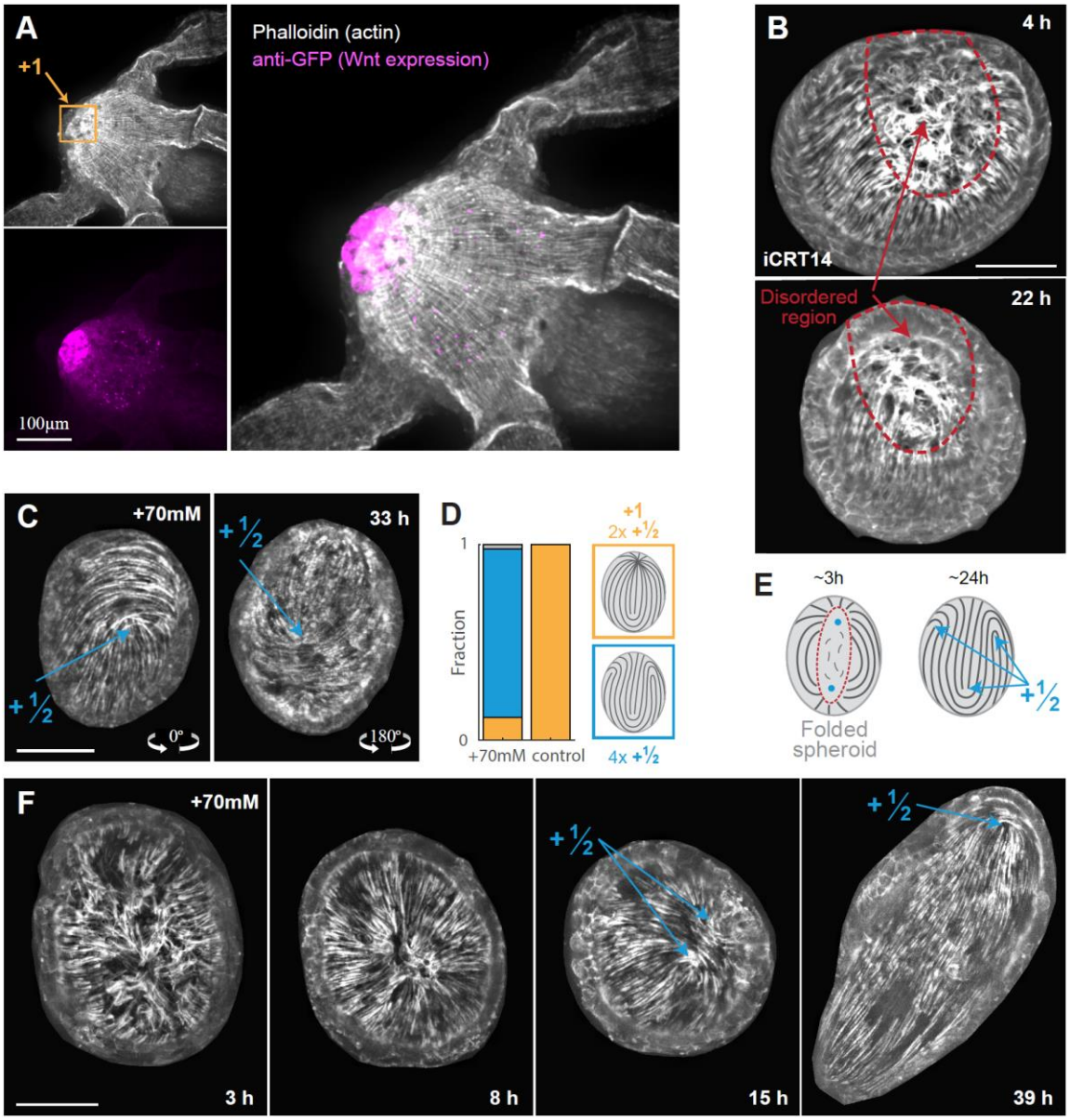

Figure 6. Perturbations of the Wnt signaling pathway and their influence on actin fiber dynamics and tissue deformations. *(A) Images of the head region in a fixed mature Hydra. Transgenic Hydra from a Wnt-expression reporter strain are fixed and stained with anti-GFP to visualize Wnt expression and with phalloidin to visualize the ectodermal and endodermal actin fibers (Methods). The coincidence of the region with Wnt expression and the +1 defect site in the actin fiber organization is evident. (B) The effect of Wnt inhibition with iCRT14 on actin fiber organization (Methods). Images from a time-lapse movie of a regenerating fragment, treated with 5µM iCRT14, taken at an early (top) and later (bottom) time point (Movie 9). While the inherited aligned fibers are maintained, new fibers do not form in the disordered region (red line) and point defects do not emerge. (C-F) The effect of elevated medium osmolarity on actin fiber organization. Tissue fragments are excised and allowed to seal in normal medium for 3-4 hours, and subsequently placed in isotonic medium containing 70mM sucrose (Methods). (C) Images from opposite sides showing a Hydra tissue spheroid placed in isotonic medium. The spheroid displays a pair of +½*

defects on both sides, forming a 4x +½ defect configuration. (D) Bar plot comparing the defect configurations observed in isotonic medium after 24-48 hours to control conditions. (E) Schematic illustration of the actin fiber organization in the folded spheroid and following the induction of order in a Hydra tissue spheroid placed in isotonic medium. The actin fibers reorganize into a nematic array in the initially disordered region, and form a 4x +½ defect configuration. (F) Images from a time-lapse movie in isotonic media (Movie 10) showing a disordered region that rapidly orders into a +1 defect (8h), that is unstable and subsequently unbinds into a pair of +½ defects (15h). The tissue spheroid stabilizes in a 4x +½ defect configuration and elongates along the fibers' direction (39h).

Mechanochemical model of Hydra regeneration

Our results show that the actomyosin muscle fiber patterns lead to focusing of mechanical strain at a specific location upon activation of contraction (Figs. 2,3,5). Notably, the site of mechanical strain focusing can be identified in the folded spheroid from the onset of the regeneration process and coincides with the location of the emergence of the future head organizer at the tip of the regenerating head (Fig. 1). Given that the formation of an aster-shaped +1 defect and the emergence of a new head organizer occur at the same location (Fig. 6A), likely within the first 24 hours after excision, an obvious question that arises is whether and how these events are related to each other.

We propose a self-organized mechanism whereby the mechanical focusing at the focal point of the actin fiber organization and the focusing of biochemical signals required for the establishment of the new head organizer reinforce each other to guide the robust formation of a head organizer (Fig. 7A). Specifically, we suggest a closed-loop feedback in which localized strain generated at the foci of the actin fibers drives morphogen production at these sites. Concurrently, regions of high morphogen expression direct the alignment of the actin fibers along morphogen gradients and stabilize aster-shaped +1 defects. Together, these generate a positive feedback loop, where mechanical strain focusing creates a localized source for morphogen production which in turn directs fiber organization around it, further enhancing the local strain focusing at this site.

While the mechanistic details that could produce this proposed self-organization mechanism are unknown, recent results by us and others support different parts of the proposed feedback loop. Our results here show that the location of the future head organizer in regenerating fragments can be identified from the fiber pattern at the onset of the regeneration process (Fig. 1), prior to the localization of head-specific biochemical signaling activity (Suzuki et al., 2023). The relation between mechanical strain and Wnt production was recently suggested by Ferenec *et al*., who correlated the reduced tissue stretching in regenerating Hydra tissues under isotonic conditions with their inability to stabilize Wnt expression and regenerate a head (Ferenc et al., 2021). Note that in that work, the mechanical strain experienced by the tissue was assumed to be spatially homogenous, whereas our high-resolution imaging reveals that mechanical strain is focused at the future organizer site. Finally, the idea that morphogen gradients can direct the orientation of actin fibers was recently suggested theoretically (Wang et al., 2023c), and is supported by observations showing that local Wnt expression can induce the formation of aster-shaped +1

defects during budding or in grafting experiments (Aufschnaiter et al., 2017; Wang et al., 2020). This notion is further supported by our current results showing the inability to stabilize aster-shaped +1 defects following perturbations of the Wnt pathway (Fig. 6).

We examine the feasibility of the proposed self-organization mechanism to produce a stable organizer, consisting of a morphogen peak at the site of an aster-shaped +1 defect, by developing a biophysical model of regenerating Hydra tissue dynamics (Fig. 7; see Supplementary Information for details). This model extends the description of Hydra tissue mechanics (Fig. 5), by including the coupled dynamics of the nematic field describing the orientation of the actomyosin fibers and a biochemical morphogen throughout the regeneration process. The morphogen field is defined by specifying the number of molecules N_i in each cell i. Molecules diffuse down the concentration gradient between cells, and are degraded at a constant rate r_- (Fig. 7B). We introduce a strain dependent morphogen source term as a sigmoid function of cell area strain, characterized by a threshold cell area strain value ε_{th} and a saturation level r_+ (Fig. 7B, Supplementary Information). The dynamics of the nematic field are governed by an interaction term that tends to align fibers in neighboring cells, as well as a coupling of the fiber orientation to local morphogen gradients (Fig. 7B, Supplementary Information). The neighbor nematic interaction favors the lowest-charged +½ defects, and competes with the alignment to morphogen gradients that stabilizes +1 defects at morphogen peaks (Wang et al., 2023c). The recurring transient actomyosin fiber contractions are emulated by periodically turning on the active stress in all cells with a period T_ζ and a magnitude ζ_M using a Gaussian profile in time of width ΔT_ζ.

Using this model, we simulate the dynamics of the regeneration process starting from a tissue spheroid, with an initial fiber configuration that has a large disordered region with an overall nematic charge +2 (as in Fig 5B) and no morphogen. We evolve the full dynamics of the vertex model together with the morphogen and nematic fields through a series of global fiber contraction activation cycles, and examine whether the disordered region can reliably resolve to form a +1 nematic defect colocalized with a morphogen peak. We find model parameters that reproduce the emergence of a +1 defect in the nematic alignment that coincides with the center of a pronounced peak in morphogen concentration (Figs. 7C, Movie 11; see SI for technical details). Moreover, we find a pair of +½ defects emerging on the other side, as observed during Hydra regeneration. Interestingly, for the same set of model parameter, different random initializations of the nematic orientation in the disordered region can also yield a spheroid with two morphogen peaks coinciding with two +1 defects (Fig. 7C, Movie 12). Thus, while the suggested feedback loop appears to robustly produce at least a single “head organizer” (i.e. a region containing a morphogen peak and an aster-shaped defect in the fiber pattern), it does not prevent the formation of two organizer sites. We further find, as expected, that +1 defects cannot be stabilized in simulations with no morphogen production (effectively corresponding to an infinitely-high value of the strain threshold ε_{th}), and only +½ defects emerge (Fig. 7C, Movie13). The outcome defect configuration varies as the strain threshold value is reduced, with four +½ defects being most common at high values of ε_{th}, and two +1 defects being most common at low values (Fig. S6). A full analysis of this model will require further work to provide a detailed characterization of the phase space for regeneration outcome as a function of model parameters.

A Organizer formation as a self-organization process

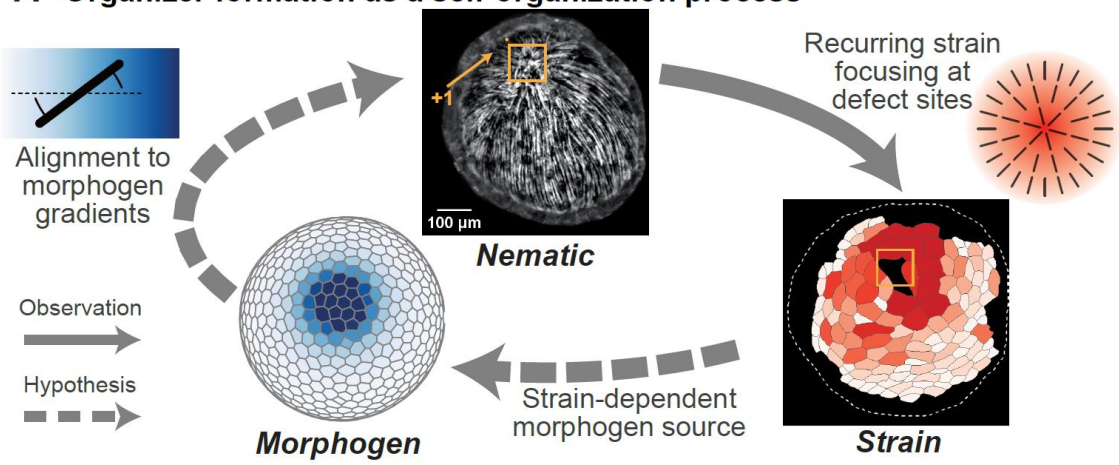

B Model of morphogen and nematic dynamics

Nematic $$\dot{\boldsymbol{q}}_c = \underbrace{\frac{1}{\tau_q}\langle \boldsymbol{q}\rangle_c}_{\text{Neighbor alignment}} + \underbrace{\alpha\left(\vec{\nabla}\phi_c \otimes \vec{\nabla}\phi_c\right)^{ST}}_{\text{Morphogen gradient alignment}} + \underbrace{m(\boldsymbol{q}_c)\boldsymbol{q}_c}_{\text{Normalization constraint}}$$

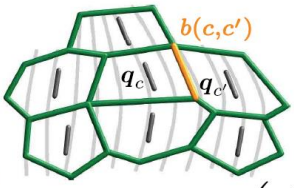

Area strain $\epsilon_c = \ln\left(\frac{A_c}{A_c^{\text{ref}}}\right)$

Morphogen

$$\phi_c = \frac{N_c}{A_c} \qquad \dot{N}_c = \underbrace{D\sum_{c'} L_{b(c,c')}\left(\phi_{c'} - \phi_c\right)}_{\text{Diffusion}} - \underbrace{r_- N_c}_{\text{Degradation}} + \underbrace{r_+ f\left(\langle\epsilon\rangle_c\right)}_{\text{Production}}$$

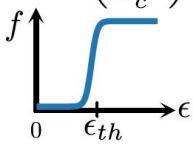

C Simulations of Hydra regeneration model

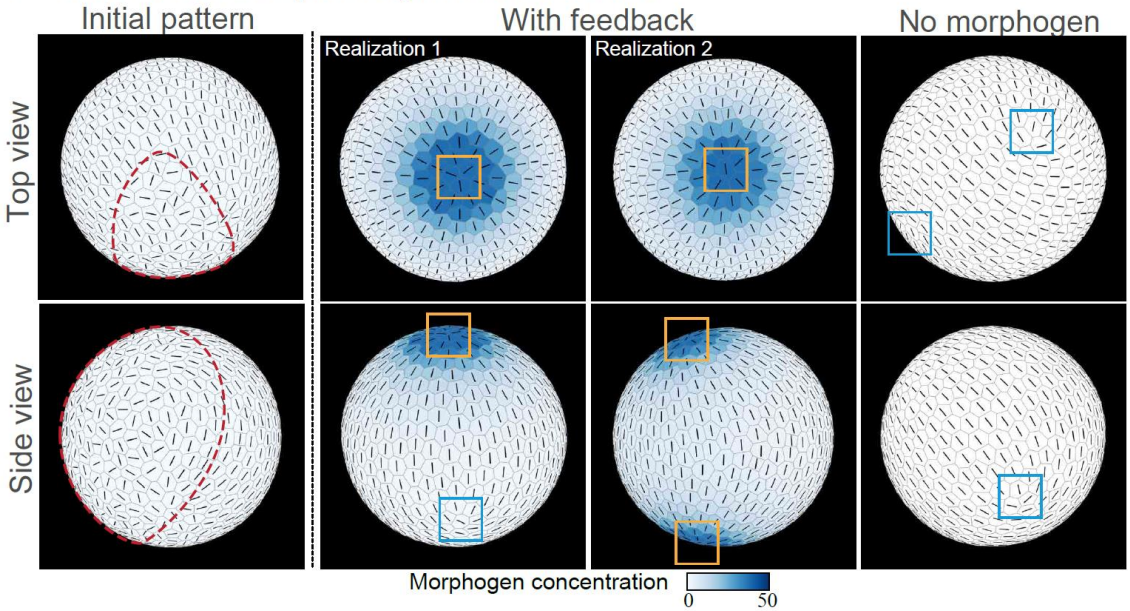

Figure 7. Biophysical model of Hydra tissue regeneration coupling tissue mechanics and morphogen dynamics. *(A) Schematic illustration of the closed-loop feedback relating dynamics of the nematic field describing the actin fiber organization, the tissue strain field and a morphogen concentration field. Mechanical strain focusing induces local morphogen production. The actin fibers tend to align along the direction of morphogen gradients, enhancing the mechanical strain focusing at defect sites, and closing a positive feedback loop. (B) Equations describing the dynamics of the nematic and morphogen concentration fields in the model of Hydra regeneration. The nematic field (*$\boldsymbol{q_c}$*) represents the local orientation of the actin fibers that tend to align to fibers in neighboring cells and to the local morphogen gradient. The dynamic of the morphogen include diffusion between cells, degradation at a constant rate and a mechanical strain-dependent production term described by* $f(\epsilon_{th})$*, where* ϵ_{th} *is the cell area strain. Here,* N_c *is number of morphogen molecules in a cell,* D *is an effective diffusion coefficient,* $L_{b(c,c')}$ *is length of the bond shared by cell* c *and its neighbor* c'*, and* $\phi_c = N_c/A_c$ *is the average morphogen concentration in a cell.* r_- *and* r_+ *are the morphogen degradation and production rates. The time-scale* τ_q *characterizes the nematic neighbor alignment rate,* $m(\boldsymbol{q}_c)$ *is a Lagrange multiplier used to constrain the nematic magnitude to unity, and* α *characterizes the alignment of nematic to the morphogen gradient. The model considers recurring global contraction activation cycles that are described by introducing a time dependent active stress as in Fig. 5. For further details, see Methods and Supplementary Information. (C) Simulation results showing regenerating tissue spheroids initiated with a partially ordered fiber configuration (as in 5B) and no morphogen (left panel; see SI for details). The tissues self-organizes into a configuration with a +1 defect colocalized with a morphogen peak at one end of the spheroid (emulating the organizer emerging at the future head site), and a pair of +½ defects at the opposite side (Movie 11), or into a configuration with two +1 defect colocalized with morphogen peaks on opposite sides (middle panels; Movie 12). These distinct outcomes arise from simulations using the same model parameters but having different realizations of the nematic in the disordered region in the initial conditions (Fig. S6). Simulations with no morphogen production develop a four +½ defect configuration (right panels; Movie 13).*

DISCUSSION

The initial configuration of supracellular actin fibers in regenerating Hydra tissue spheroids depends on the inherited fiber organization in the excised tissue fragments and the pattern of tissue folding. Here we show that the folding process robustly generates a nematic configuration that contains two discrete actin foci, which can be identified in the folded spheroid early on, and persist throughout the regeneration process (Fig. 1). We find that these actin foci develop into a characteristic set of topological point defects in the nematic field, that eventually coincide with the sites of head and foot formation in the regenerated animal. As such, the location of the future head/foot can be identified from the actin fiber pattern at the onset of the regeneration process, and contrary to previous claims (Soriano et al., 2009) are not associated with a spontaneous symmetry breaking. We further show that these actin foci experience recurring localized tissue stretching and rupture events (Fig. 2-4). The mechanical strain focusing at defect sites arises from transient activation of the actomyosin fibers, which contract and generate in-

plane stress in the tissue that becomes focused at defect sites, simply because of their structure (Fig. 5). The magnitude of stress generated at these foci is considerable and produces an appreciable (~2-fold) increase in cell areas, generating a unique, local mechanical signature at the future head site that is evident despite the presence of extensive disorder and fluctuations in the tissue (Fig. 3).

Hydra has been a classic model system for studying axial patterning during animal morphogenesis for over a century, since the pioneering work of Ethel Brown who discovered the head organizer in Hydra (Bode, 2012; Browne, 1909). Subsequent work established the presence of head-inducing activation and inhibition activities that are graded along the body axis (Shimizu, 2012). These observations led to the development of the famous Gierer-Meinhardt model that describes axial patterning in Hydra as a reaction-diffusion process, involving a diffusible activator and inhibitor, whose production is governed by a slowly-varying source density field (Meinhardt, 2012b). This model successfully integrated a large body of observations from grafting and regeneration experiments into a coherent picture that has dominated the field, in which tissue-scale gradients of the activator and inhibitor generate short-range activation and long-range inhibition of head formation. Despite its popularity, the mechanistic basis for this model is still unclear, and in particular, the nature of the source term that is a crucial ingredient of the model has remained obscure (Meinhardt, 2012a; Wang et al., 2023b). In the context of our work, it is also important to note that the Gierer-Meinhardt model emphasizes the role of diffusible morphogens, but does not consider the possible contribution of mechanics and the nematic fiber organization to the patterning process (Maroudas-Sacks et al., 2024).

Our high-resolution imaging of regenerating Hydra revealed the highly dynamic and inhomogeneous tissue deformations that occur during the regeneration process (Figs. 2-4). This enabled us to identify the coupling between the nematic actin fiber organization and the tissue deformations, and in particular the correlation between defect sites in the nematic field and transient localized peaks in the tissue strain field. While the activation of the Hydra actomyosin fiber contraction via calcium excitations exhibits rich spatiotemporal dynamics in the developing tissue (Agam and Braun, 2023), our observations indicate that the most prominent deformations correspond to essentially global activation of actomyosin fiber contraction that lead to a characteristic tissue-scale deformation pattern with focused area strain at defect sites.

Theoretically, the stable defect configuration for a nematic field on a spheroid is expected to contain four +½ defects (Shin et al., 2008). This defect configuration is distinct from the characteristic defect pattern found in regenerating Hydra fragments, which typically contains a +1 defect at the future head and a pair of +½ defects at the future foot (Fig. 1). As previously suggested (Wang et al., 2023c), +1 defects can be stabilized through a coupling of the nematic field to gradients of a morphogen field (Fig. 7). Interestingly, we observe that spheroids placed in elevated osmolarity, under conditions where Wnt signaling is suppressed (Ferenc et al., 2021), develop a four +½ defect configuration (Fig. 6C,D). Moreover, even if a +1 defect appears during the induction of order in the initially disordered region, it is unstable and unbinds into a pair of +½ defects (Fig. 6E). As such, our results demonstrate that stable +1 nematic defect are not a necessity of the nematic alignment interaction in Hydra, but rather require some additional

stabilizing interaction. We hypothesize that this additional coupling is part of a mechanochemical feedback involved in head organizer formation.

Ferenc *et al.* recently suggested that tissue stretching due to osmotic inflations (which are absent under isotonic conditions) are essential for regeneration because of their role in stabilizing Wnt expression (Ferenc et al., 2021). While we believe that their results are valuable in highlighting the importance of mechanochemical coupling involving the Wnt pathway in Hydra regeneration, we disagree with the suggested interpretation. Indeed, the saw-tooth pattern in tissue area dynamics, which is associated with cycles of large osmotic inflations and ruptures (Ferenc et al., 2021; Kucken et al., 2008), is typically observed in regenerating Hydra spheroids. However, contrary to previous claims, this pattern is not essential for regeneration. Specifically, we observe spheroids under normal conditions that exhibit one large inflation or even no appreciable inflation (likely due to being more prone to tissue rupture) and yet regenerate normally (Fig. S7). Similarly, we have previously shown that tissue pieces regenerating on thin wires that pierce the tissue and generate a leaky spot, exhibit tissue dynamics with a few or no saw-tooth yet are still able to regenerate (Livshits et al., 2017). Furthermore, according to Ferenc and coworkers, the homogenous stretching during osmotic inflations would be expected to generate broad Wnt expression in the tissue spheroid. The localized Wnt expression found at the future head site, was attributed to random symmetry breaking. However, our work shows that the location of the future head is specified from the onset of the regeneration process (Fig. 1D) (Shani-Zerbib et al., 2022), so the location of the regenerated head reflects an inherited asymmetry rather than random symmetry breaking.

We suggest a closed-loop positive feedback that couples topological defects in the nematic field with localized morphogen production, via the spatiotemporal patterns of the tissue strain generated during actomyosin fiber contraction (Fig. 7). Within our model, the observed emergence of a new head organizer at the defect site is not a coincidence or a corollary of a biochemical patterning mechanism. Rather, we suggest that head organizer formation reflects a dynamic self-organization process that involves an interplay between morphogen dynamics and the nematic field. This hypothesis is appealing, since it naturally provides a mechanism for inducing local organizer activity. The nematic field robustly generates discrete foci (defects) that produce highly localized strain. The slow dynamics of the morphogen source in this picture, arise from the stability of the actin fiber pattern that is observed to be a slowly-varying field in regenerating Hydra (Maroudas-Sacks et al., 2021).

Obviously the formation of a new organizer is not solely determined by this mechanical coupling. The Wnt signaling pathway has been shown to be controlled by a autocatalytic regulatory network and exhibit non-linear dynamics that can generate localized production on their own (Nakamura et al., 2011). Moreover, the memory of polarity that is evident in regenerating tissues implies the presence of additional relevant fields (Javois et al., 1988; Shani-Zerbib et al., 2022) (Fig. 1). While our current model of morphogen field dynamics is too simplistic, we believe that the proposed mechanochemical coupling between the Wnt signaling pathway and the nematic field, plays a role in facilitating the robust yet highly flexible ability of Hydra to regenerate and establish a new head organizer. Interestingly, similar mechanochemical coupling has been shown to be important in regenerating jellyfish fragments, where reorganization of the muscle fibers into aster-shaped defects was shown to define structural

landmarks for the formation of the Wnt signaling center at the future manubrium (Sinigaglia et al., 2020).

The proposed mechanochemical feedback seems particularly important in regeneration from excised tissue pieces. Unlike grafting experiments or bud formation, where the morphogenesis process and defect formation initiate in a region that contains a pre-established morphogen peak (Hobmayer et al., 2000), regenerating fragments are not expected to possess a well-defined initial biochemical pattern (Suzuki et al., 2023). The excised tissue spans only a small fraction of the body length of the parent animal and folds so that its originally head and foot-facing sides adhere to each other, making it unlikely that the folded spheroids contain a clear morphogen peak that emanates from morphogen gradients in the parent animal. Similarly, the possibility that the site of head formation is specified by a localized wound response (as seems to be the case in bisected animals (Cazet et al., 2021; Gufler et al., 2018)) appears unlikely, since the excised tissue fragment is wounded from all directions and folds into a spheroid in which the closure region spans nearly half of the regenerating spheroid (Fig. 1). Nevertheless, our observations show that head formation in regenerating tissue fragments occurs in a well-defined location that can be identified from the actin fiber pattern at the onset of the regeneration process. Our ability to precisely specify this location and identify a unique mechanical signature at that site (namely, recurring localized stretching events that do not occur elsewhere in the tissue), highlights the strong coupling between mechanics and the biochemical signaling processes associated with organizer formation.

In the context of regenerating fragments, we suggest that the mechanical fields can play an instructive role in specifying the future head site (Fig. 7). However, importantly, the relation between the presence of nematic defects and the establishment of a head organizer is not a simple causal relation. The proposed mechanism involves a feedback loop coupling the morphogen field and the nematic field, where neither is upstream or downstream from the latter (Fig. 7A). We suggest that the patterning process is dynamic, and that depending on the context, different aspects of the initial conditions can be more or less instructional in guiding the highly flexible yet robust regeneration process. The memory of polarity, even in small excised tissues (Javois et al., 1988; Shani-Zerbib et al., 2022), in this view, does not arise from a well-defined pre-pattern, but rather emerges dynamically from the amplification of small initial biases that are present in the excised tissue in a consistent enough manner.

This work is only an initial step in deciphering the mechanochemical coupling underlying axial patterning in Hydra. We show that the nematic actin fiber organization generates mechanical strain focusing at defect sites and suggest a mechanism where the localized strain effectively acts as a morphogen source term. We use biophysical simulations to show that this model can theoretically produce a site with colocalization of a morphogen peak and a +1 defect, as observed in the head of the regenerated Hydra (Fig. 6A). While our proposed mechanochemical model is consistent with various experimental observations and has attractive features, it is nonetheless still speculative. Future work is required to establish this model from a phenomenological point of view, by proving that this model can predict the behavior of regenerating tissues from a variety of initial conditions (Livshits et al., 2017) and under different mechanical and biochemical perturbations (Maroudas-Sacks et al., 2024; Wang et al., 2020).

From a mechanistic point of view, activation of contraction in the nematic actomyosin fibers appear to nicely account for the observed relation between the nematic field and the tissue strain field (Fig. 5). However, the mechanisms that relate the strain field and the morphogen field as well as the influence of morphogen gradients on actin fiber organization are still unknown. Tissue stretching has been shown in other systems to activate biochemical signaling (Martino et al., 2018). In particular, the Hippo-YAP pathway is known to respond to a diverse set of mechanical cues (Panciera et al., 2017), and is coupled to the Wnt signaling pathway (Azzolin et al., 2014). Similarly, while the Wnt pathway has been shown to influence actin dynamics (Stamatakou et al., 2015), how this could lead to nucleation and alignment of myonemes in Hydra remains unknown.

Our suggested mechanochemical model for Hydra morphogenesis bears similarities with emerging views of plant morphogenesis, where mechanical forces have been shown to play an instructional part in the patterning process through mechanochemical feedback that couple cytoskeletal alignment, mechanical stress/strain fields and the distribution of morphogens such as Auxin (Trinh et al., 2021). We believe that such self-organized dynamics involving mechanochemical feedback between stresses generated by the actomyosin cytoskeleton and signaling pathways are broadly relevant for animal morphogenesis. More generally, the presence of feedback from the emerging structure back into the patterning process itself naturally provides developing systems with immense flexibility, while at the same time promoting the emergence of robust outcomes with well-defined patterns.

MATERIALS AND METHODS

Hydra strains culturing and regeneration from tissue fragments

All the experiments are performed using transgenic Hydra strains expressing Lifeact-GFP in the ectoderm, generously provided by Prof. Bert Hobmayer (University of Innsbruck, Austria). Additionally, we use a Wnt expression reporter strain, HyWnt3:GFP-HyAct:dsRED transgenic strain (Nakamura et al., 2011; Vogg et al., 2019) }, kindly provided to us by Prof. Brigitte Galliot's lab (Geneva University, Switzerland), for studying Wnt expression in fixed Hydra (Fig. 6A). Animals are cultured in standard Hydra culture medium (HM: 1mM $NaHCO_3$, 1mM $CaCl_2$, 0.1mM $MgCl_2$, 0.1mM KCl, 1mM Tris-HCl pH 7.7) at 18° C. The animals are fed 3 times a week with live Artemia Nauplii and rinsed after 4-8 hours. Tissue fragments are excised from the middle body section of mature Hydra, ~24 hours after feeding, using a scalpel equipped with a #15 blade. Tissue rings are excised by performing two nearby transverse cuts, and are subsequently cut into two to four parts by additional longitudinal cuts to obtain rectangular tissue pieces.

Tissue labelling

To label specific tissue regions we use laser-induced activation of a caged dye (Abberior CAGE 552 NHS ester) that is electroporated uniformly into mature Hydra and subsequently uncaged in the desired region (Maroudas-Sacks et al., 2021; Shani-Zerbib et al., 2022). Electroporation of the probe into live Hydra is performed using a homemade electroporation setup. The electroporation chamber consists of a small Teflon well, with 2 perpendicular Platinum electrodes, spaced 2.5 mm apart, on both sides of the well. A single Hydra is placed in the chamber in 10µl of HM supplemented with 6-12mM of the caged dye. A 75 Volts electric pulse is applied for 35ms. The animal is then washed in HM and allowed to recover for several hours to 1 day prior to tissue excision. Following excision, the specific region of interest is activated by a UV laser in a LSM 710 laser scanning confocal microscope (Zeiss), using a 20× air objective (NA=0.8). The samples are first briefly imaged with a 30 mW 488 nm multiline argon laser at up to 1% power to visualize the Lifeact-GFP signal and identify the region of interest for activation. Photoactivation of the caged dye is done using a 10 mW 405nm laser at 100 %. The activation of the Abberior CAGE 552 is verified by imaging with a 10 mW 543 nm laser at 1%. Subsequent imaging of the Lifeact-GFP signal and the uncaged cytosolic label is done by spinning-disk confocal microscopy as described below.

Fixation and immunofluorescence staining

Intact Hydra from the HyWnt3:GFP-HyAct:dsRED transgenic strain are relaxed in 2% urethane in HM for one minute, and fixed in 4% formaldehyde in HM for 1 hour at room temperature. Samples are permeabilized with 0.1% Triton-X100 in PBS (PBT; 3 washes X 5 min) and then incubated for 2 hours with 0.1 % Triton-X100, 3% Bovine serum albumin (BSA, w/v) in PBS (PBSBT). For staining, samples are incubated with an AlexaFluor 647-conjugated anti-GFP, rabbit polyclonal antibody (2 mg/ml; Invitrogen) and AlexaFluor 488-conjugated phalloidin (200u/ml; Invitrogen) diluted 1:1:100 in PBSBT, and incubated overnight at room temperature with gentle shaking. Subsequently, samples are washed three times in PBT (3 washes X 15 min) and then in PBS (3 washes X 5min). Each sample is then placed in a cube of 2% low gelling agarose (sigma)

and the cube is placed on a coverslip with its head facing the objective in order to image the mouth region.

Sample preparation

Time-lapse live imaging is performed either in HM or in soft gel (0.5% low gelling point agarose (Sigma) prepared in HM to reduce tissue movement during imaging. The general characteristics of the regeneration process in soft gel are similar to regeneration in aqueous media. Samples are made in 50mm glass-bottom petri dishes (Fluorodish), polymer coverslip 24-well plates (Ibidi µ -plate 24 well, tissue culture treated), or in custom-made sample holders with a coverslip bottom. The samples are placed in few-mm sized wells cast of 2% agarose (Sigma) prepared with HM. For experiments in gels, the regenerating tissues are placed in liquefied 0.5% low gelling agarose gel that is cool enough not to damage the samples (~ 35°C), ~ 3-6 hours after excision (to allow the tissue pieces to first fold into spheroids), and the gel subsequently solidifies around the tissue. We add a few mm of HM above the gel to ensure it does not dry out during imaging.

To image samples from all directions by spinning-disk confocal microscopy, regenerating tissues are loaded within soft gel into FEP tubes (which have a similar refractive index to the surrounding solution) with a square cross-section and an internal diameter of 2 mm (Adtech). As above, the samples are inserted in liquefied 0.5% low gelling agarose gel and positioned within the FEP tubes. During imaging, the tubes are manually rotated to each of the 4 flat facets of the square tube and secured using a homemade Teflon holder to keep them stationary at each orientation. Images from 4 directions are acquired at the specified time points.

Samples for the up-and-under spinning-disk confocal microscope are prepared as follows. When using two air objectives, the samples are sandwiched between two glass coverslips at a set distance apart that are sealed from the environment to prevent leaks and fluid evaporation. The samples are placed within 2% agarose wells, which are filled with 0.5% low gelling agarose gel around the samples to maintain an aqueous environment between the coverslips. When using an air objective from below and a dipping lens from above, the samples are placed in a 50mm glass-bottom petri dish (Fluorodish) equipped with a homemade Teflon ring with tubing to allow perfusion of media to prevent evaporation. The samples are placed in wells made from 2% agarose that are filled with 0.5% low gelling agarose gel. When using the gel, the samples are layered with 3-4 ml of media on top of the gel. On the microscope stage we connect the small tubes from the Teflon ring to a peristaltic pump (Ismatec) and slowly flow media over the samples.

Samples for the light-sheet microscope are loaded in liquefied 0.5% low gelling agarose gel into a ~ 1 cm long cylindrical FEP tube with an internal diameter of 2.15 mm (Zeiss Z1 sample preparation kit) and positioned along the central axis of the tube. The imaging is done through the FEP tubing, which has a similar refractive index to the surrounding solution.

Pharmacological and osmotic perturbations

Pharmacological inhibition of the Wnt pathway with iCRT14 is done as follows (Cazet et al., 2021). Parent animals are preincubated in 5µM iCRT14 (sigma #SML0203) in HM for 2 hours prior to excision. Tissue fragments are cut and left to seal for ~3 hours in the same solution

(5µM of iCRT14 in HM). Tissue spheroids are then placed in wells prepared from 2% agarose containing 5µM iCRT14, and embedded in 0.5% low gelling agarose gel containing 5µM of iCRT14, and further layered with 5µM of iCRT14 in HM. The media with iCRT14 is refreshed every 24hr.

Perturbations with isotonic media (Ferenc et al., 2021) are done as follows. Tissue fragments are excised and allowed to seal for 3 hours in normal HM. Tissue spheroids are then placed in wells prepared from 2% agarose containing 70mM Sucrose (sigma, #84097), and embedded in 0.5% low gelling agarose gel containing 70mM Sucrose, and further layered with HM containing 70mM Sucrose with constant perfusion.

Microscopy

Spinning-disk confocal z-stacks are acquired on a spinning-disk confocal microscope (Intelligent Imaging Innovations) running Slidebook software. The Lifeact-GFP is excited using a 50mW 488nm laser and the activated Abberior CAGE 552 is excited using a 50mW 561nm laser. Images are acquired with an EM-CCD (QuantEM; Photometrix). Time-lapse movies of regenerating Hydra are taken using either a 10× air objective (NA=0.5), a 10x water objective (NA=0.45), or a 20x air objective (NA=0.75).

The up-and-under setup is a custom, double spinning-disk confocal microscope (Intelligent Imaging Innovations) running Slidebook software, which enables imaging of the sample from two opposing angles - above and below. The Lifeact-GFP is excited using a 50mW 488nm laser and the activated Abberior CAGE 552 is excited using a 50mW 561nm laser. Images are acquired with two sCMOS cameras (Andor Zyla 4.1). Time lapse movies of regenerating Hydra are taken using a 10x air objective (NA=0.5) or a 20x air objective (NA=0.75) from below, and a 10x air objective (NA=0.3) or a 20x dipping lens (NA=0.5) from above.

Light-sheet microscopy is done on a Lightsheet Z.1 microscope (Zeiss). The light-sheet is generated by a pair of 10x air objectives (NA=0.2), imaged through 20× water objectives (NA=1), and acquired using a pair of CMOS cameras (PCO.edge). The Lifeact-GFP is excited using a 50mW 488nm laser and the activated Abberior CAGE 552 is excited using a 50mW 561nm laser. 4 views from different angles are acquired for the same sample by rotating the specimen. The imaging is performed using the “pivot scan” setting to minimize imaging artefacts that introduce streaking in the direction of illumination, yet some remnants of the streaking artefacts are still apparent in the images.

All 3D stacks in the spinning-disc microscopy systems and light sheet microscope are acquired at room temperature, typically taken at 3µm z-intervals. The time resolution of the movies ranges from 20 seconds to 30 minutes depending on the experiment. Imaging is done using appropriate emission filters at room temperature.

Time-lapse epifluorescence and bright field movies of regenerating Hydra are recorded on a Zeiss Axio-Observer microscope with a 5× air objective (NA = 0.25), at room temperature. Images are acquired on a charge-coupled device (CCD) camera (CoolSnap, Photometrix), and illuminated with a Xenon lamp. Time lapse imaging begins ~ 4.5 hours after excision. and continues for 3 days at a time interval of 10 minutes.

Image processing and analysis

The tools used for image processing and analysis are based on a combination of custom-written code with adaptation and application of existing algorithms, written in MATLAB, Python and ImageJ, as detailed below.

Creating masks of tissue region

In order to define the image region for analysis, masks were generated for every image based on the maximum intensity projections of the Lifeact-GFP signal, using automatic thresholding in ImageJ ('Li' method), and performing morphological operations (erosion, dilation, hole-filling) in MATLAB to obtain masks that accurately mark the tissue region in the image. All subsequent analysis was performed for the regions within the tissue masks.

Surface detection and layer separation

The regenerating Hydra tissue spheroids consist of a bilayered epithelium surrounding a hollow cavity. The 2D apical and basal surfaces of the ectoderm are computationally identified in the 3D fluorescence z-stacks of the Lifeact-GFP signal in the ectoderm. The supracellular actin fibers reside on the basal surface of the ectoderm while the apical junctions marking the cell outlines are visible on the apical surface. 2D projected images of the basal and apical surfaces of the ectoderm are automatically extracted from the 3D spinning-disk z-stack acquired with a 3µm z-interval using the "Minimum Cost Z surface Projection" plugin in ImageJ (https://imagej.net/Minimum_Cost_Z_surface_Projection). The cost images are generated by pre-processing the original z-stacks using custom-code written in MATLAB. First, the signal from the ectoderm layer was manipulated to make it more homogeneous within the layer without increasing its thickness, by applying the built-in MATLAB anisotropic diffusion filter. Subsequently, we employ a gradient filter to highlight the apical and basal surfaces as the top and bottom boundaries of the ectoderm layer. The apical and basal surfaces are determined using the minCost algorithm (Parameters used: Rescale xy: 0.5, rescale z: 1, min distance: 15µm, max distance: 45µm, max delta z: 1, two surfaces). The surfaces given by the minCost algorithm are then smoothed by applying an isotropic 3D Gaussian filter of width 1-3 pixels (after rescaling to an isotropic grid matching the resolution in the z-direction) and selecting the iso-surface with value 0.5.

Image projection

2D projected images of the ectodermal actin fibers that reside on the basal surface of the ectodermal layer and the apical junctions, which are visible on the apical surface are generated by extracting the relevant fluorescence signal from the 3D image stacks based on the smoothed basal and apical surfaces determined above, respectively. For each x-y position, we employ a Gaussian weight function in the z-direction with a sigma of 3µm, which is centered at the z-value determined from the smoothed surface. The resulting 2D projected images are further subject to contrast limited adaptive histogram equalization (CLAHE) with MATLAB's "adapthisteq" function with Rayleigh distribution and a tile size of 26µm. 2D projection of the photoactivated

dye are generated by taking a maximum intensity projection of the 3D image stacks in the z-region between the smoothed apical and basal surface determined above.

Analysis of nematic field, defect sites and their outcome

The local orientation of the supracellular ectodermal actin fibers is described by a director field, which is oriented along the mean orientation determined in a small region surrounding every point in space. The nematic director field is determined from the signal intensity gradients in the 2D projected images of the ectodermal actin fibers, as described in (Maroudas-Sacks et al., 2021). Analysis of defect sites and their outcome in the regenerated animal is performed manually by identifying and following defects over time in 2D projections on the basal ectodermal surface 3D from fluorescent time-lapse movies of LifAact-GFP in regenerating Hydra. The defect sites included in the analysis are those that can be reliably tracked throughout the regeneration process from their formation until the final morphological outcome.

Segmentation of cell images

The contrast-enhanced apical surface images are segmented using EPySeg, a machine-learning based segmentation tool (Aigouy et al., 2020), applying a custom trained model using hand-segmented images of cell junctions as the ground truth for training. The resulting output is a binary segmentation mask for each image marking all cell outlines. The automatic segmentation is manually corrected using 'Tissue Analyzer' (Aigouy et al., 2020), also used for manual segmentation of the training set. Based on the segmentation masks, two additional output images are created for each original image using custom-written python code: an image marking all cell vertices, and an image marking all cell bonds, with each bond uniquely numbered (matching the output format of 'Tissue Analyzer').

Analysis of cell morphologies from segmented images

The segmentation masks, vertices and bond images hold the information on cell geometries and neighbor relations in the projected 2D image. This information is extracted from the images using custom written MATLAB code, and stored in a relational database format matching that of TissueMiner software (Etournay et al., 2016), with some modifications as detailed here. We apply a geometrical correction to the projected data to account for the curvature of the surface on which the cells reside, using the height map of the apical surface (see above). Since cell size is small relative to surface curvature, we assume each cell to be roughly planar in the plane tangent to the surface at the location of the cell. To determine the tangent plane for each cell, we use the mean normal to the surface over a window of width 20µm around the cell center. For each cell, we project the full cell outline from the segmented images onto the plane normal to the mean normal of the cell and subsequently smooth the resulting outline using a 5-point moving average before calculating bond lengths and cell areas to avoid artefacts due to discrete pixel resolution. 3D coordinates for cell centers, vertices and bonds (both original and smoothed), as well as neighbor relations, are stored in the database.

To query the database, quantify and visualize the data, we use a custom-written object-oriented MATLAB platform. The full documentation can be found on the lab Git repository. All geometrical measures for cells are calculated using the cell outlines on the tangent planes. Cell

geometrical measures that are calculated include area (area inside the cell's smoothed outline), perimeter (length of the smoothed outline), and cell shape anisotropy **Q**, defined as in (Merkel et al., 2017). Briefly, the cell shape anisotropy tensor **Q** is calculated by dividing each cell into triangles that connect each pair of adjacent vertices with the cell centre, and then calculating for each triangle how it differs from an equilateral triangle aligned along a set reference axis to obtain the anisotropy tensor for each triangle. For each cell, **Q** is then calculated by taking an area-weighted average over the triangles that comprise it. To calculate cell shape anisotropy along the fiber orientation, the cell shape tensor **Q** is then projected along the direction of the cell's fiber orientation. To calculate the cell shape anisotropy relative to the direction to the defect, we draw a line between the cell and defect in the 2D projected image, project this orientation to the cell plane, and project **Q** along this direction. Fiber orientation and coherence per cell are assigned by taking the mean orientation and coherence of all pixels within the cell outline. The mean fiber orientation is projected to the cell's tangent plane.

Cell's distance from defects was determined based on the graph distance, which is the minimal number of cells connecting a given cell and the cell at the center of the defect.

To calculate the logarithmic area strain at a given distance from the defect, we subtract the mean logarithm of the cell areas of all cells at that distance before the event, from the mean logarithm of the cell areas of all cells at that distance during the peak of the event. This is mathematically equivalent to calculating the mean of the logarithm of the ratio of cell area during the peak and before the event for each cell. The last frame before the deformation was determined manually, and the peak of an event was determined as the frame in which the total area of the cells within a distance of 3 cells from the defect was largest.

Analysis of local deformation and rupture event statistics

Analysis of local tissue deformation and rupture events is performed manually by identifying frames within time-lapse movies in which these events occur, using the projected images of both the apical and basal surface of the ectoderm. Events are defined as coherent tissue deformation involving dozens of cells. We record all observed events and classify them according to the pattern of deformation and its localization. Since local stretching and ruptures typically occur simultaneously at both actin foci upon contraction, more than one event is typically recorded for a single contraction, describing the deformations observed in the different tissue regions. The categories used to classify events are as follows: small local stretching (cell area increase of less than 2-fold), large local stretching (cell area change of 2-fold or more), small ruptures, large ruptures (hole diameter ~ tissue diameter), global contraction (large cell deformation in the direction perpendicular to fibers in the ordered region between the foci), and other cell shape deformations not involving area change (characterizes cell shape changes at 2x½ defect sites during global contractions). The criteria for defining a hole include a transient, visible gap in fluorescence in both the Lifeact-GFP signal and an additional tissue label if present, a change in tissue volume before and after the hole appearance and/or visible expulsion of tissue debris from the hole. Timing and location of the observed deformation and rupture events are recorded, and the sites are followed over time throughout the regeneration process (using fiduciary landmarks in the form of local photoactivated fluorescent tissue labels) to determine the fiber organization and morphological outcomes at these sites. To obtain

statistics for the cumulative event distribution over time, time-lapse movies are taken in the up-and-under system to simultaneously image the samples from above and below with a time resolution of 2-2.5 minutes, which is shorter than the characteristic duration of an event (Fig. 2F,I).

Model Simulations

In our custom vertex model of Hydra tissue mechanics, individual cells are defined by the position of their vertices. Since these vertices are in general not all in the same plane, we need to define the area and local tangent plane for each cell (Fig. S8A). To this end, we first determine the cell center, $\vec{r}_c$, as the mean position of all the cell vertices. We then define a collection of cell triangles that each contain two neighboring vertices and the cell center. The cell area is defined as the sum of all cell triangle areas. The normal vector to the cell tangent plane is defined as the area weighted average of all the cell triangle normal vectors (see SI for more details).

The vertex model energy function is defined as,

$$E = \sum_{c\in cells} \frac{1}{2}K(A_c - A_0)^2 + \sum_{b\in bonds} \Lambda\, L_b + \sum_{c\in cells} \frac{1}{2}\Gamma\, P_c^2 + \sum_{b\in bonds} \beta L_b(1 - \cos\theta_b\ ) + \mu\, V,$$

where A_c and A_0 are the cell areas and preferred cell area, K is the area elastic modulus, Λ and L_b are the bond tension and bond length, Γ and P_c are the perimeter elastic modulus and cell perimeter, β is the cell-cell bending modulus and θ_b is the angle between normal vectors of neighboring cells that share the bond b. The total volume of the lumen is denoted by V , and μ is a Lagrange multiplier that ensures lumen incompressibility.

A vertex position, $\vec{r}_i$, in the cellular network follows overdamped dynamics driven by the forces stemming from the gradient of the energy function $-\partial E/\partial\vec{r}_i$, and an active force $\vec{f}_i^a$ generated by the active stresses in all the cells to which this vertex belongs,

$$\gamma\dot{\vec{r}}_i = -\frac{\partial E}{\partial\vec{r}_i} + \vec{f}_i^a,$$

where γ is a friction coefficient. The active stress generated by a cell, $\boldsymbol{\sigma}_c^a$, stems from the contraction of the actin fibers in that cell. We introduce a unit nematic tensor $\boldsymbol{q}_c$ in the tangent plane of each cell, representing the average orientation of the actin fibers in that cell. When cells move or deform, the nematic tensor is convected and co-rotated with them (see Supplementary Information for details). We emulate global fiber contraction by simultaneously generating active stresses in all cells:

$$\boldsymbol{\sigma}_{\boldsymbol{c}}^{\boldsymbol{a}} = -\zeta(\mathrm{t})|\langle\boldsymbol{q}\rangle_{\mathrm{c}}|\boldsymbol{q}_{\mathrm{c}}\ ,$$

where the active stress magnitude $\zeta(t)$ is a Gaussian function of width ΔT_ζ that is centered at the time of the global fiber contraction and has an amplitude ζ_M.

The cellular network evolves according to the forces acting on the vertices. If at any time-step of the simulation, the length of any bond becomes smaller than a threshold value $L_c = 0.005\sqrt{A_0}$ the two vertices of that bond are merged into a single vertex and the bond disappears. In this

way 4-fold vertices are formed from merging of two 3-fold vertices. Such 4-fold vertices can resolve back into pairs of 3-fold vertices in one of two ways: reverting back to the original cellular configuration or rearranging the cells. A cell rearrangement event, also called a T1 transition, consists of the disappearance of one cell bond by the transient formation of a 4-fold vertex, that subsequently resolves into a new bond shared by cells that were previously not in contact. The stability of a 4-fold vertex is tested with respect to each of these two possible resolutions (see Supplementary Information). Note that our model supports vertices with an arbitrary large number of bonds, but in practice we observe only 4-fold vertices in our simulations.

To simulate the focusing of isotropic strain during stretching events (Fig. 5), we use a fixed nematic pattern that emulates the experimentally observed pattern of fiber alignment (Fig. 5B,C,left panels), and follow the vertex dynamics through global fiber contraction activation. Since we do not observe cell rearrangements in the Hydra ectoderm during stretching events, we chose parameters of the vertex model for which the cellular network has a negative two-dimensional Poisson ratio (see SI). This allows us to generate large isotropic strains without inducing cell rearrangements. Furthermore, we take the cell active stress amplitude to be equal to $\zeta_M = 0.5\, K\, A_0^{3/2}$, such that the isotropic strain profile we obtain in the simulation of a single event is comparable to the one experimentally observed in Hydra (Figs. 3, S4).

In order to study the proposed mechanochemical feedback between the nematic actomyosin fiber organization, mechanical strain in the tissue and morphogen concentration (Fig. 7A), we consider the coupled dynamics of the nematic field and a morphogen concentration field (Fig. 7B). The amount of morphogen in a cell c is described by the number of molecules N_c and develops over time according to,

$$\dot{N}_c = \sum_c J_{c'\to c} - r_- N_c + r_+ f(\langle\epsilon\rangle_c)\ .$$

The first term reflects the contribution of diffusive fluxes between neighboring cells, that are of the form $J_{c'\to c} = D L_{b(c,c')}(\phi_{c'} - \phi_c)$, where D is an effective diffusion coefficient that characterizes inter-cellular diffusion, $L_{b(c,c')}$ is the length of the bond shared by cell c and its neighbor c', and $\phi_c = N_c/A_c$ is the average morphogen concentration inside the cell. In this model intra-cellular diffusion is assumed to be much faster than transport between cells, so the morphogen concentration at the interface between two cells can be approximated by the average cellular concentration, ϕ_c. Furthermore, we assume that the morphogen is degraded at a constant rate r_- ,and produced at a rate that is an increasing function of the cell area strain $\epsilon_c = \ln\left(A_c/A_c^{ref}\right)$, where A_c^{ref} is the initial cell area at t=0. We use a sigmoid production function $f(\epsilon_c) = 1/2\ \tanh(w(\epsilon_c - \epsilon_{th})/\epsilon_{th})$, with $w = 10$, so that f increases sharply as a function of the strain around the threshold strain value ϵ_{th}. Therefore, the production is small below ϵ_{th} and quickly saturates to r_+ above it. Note that, without loss of generality, we can set $r_+ = 1$, which corresponds to expressing N_c in units of r_+/r_- . The morphogen dynamics equation is therefore characterized by a degradation time-scale $\tau_- = 1/r_-$ and a length-scale $\lambda = \sqrt{D A_0^{1/2}/r_-}$, which reflects the length scale a morphogen diffuses before degrading.

To describe dynamics of the nematic field, we assume that the nematic orientation in each cell is coupled to the nematic orientation in neighboring cells, and we further introduce a coupling of the nematic to the local morphogen concentration gradient,

$$\dot{\boldsymbol{q}}_c = \frac{1}{\tau_q}\langle \boldsymbol{q}\rangle_c + m(\boldsymbol{q}_c)\boldsymbol{q}_c + \alpha\left(\vec{\nabla}\phi_c \otimes \vec{\nabla}\phi_c\right)^{ST}.$$

Here, the neighbor alignment is introduced through the average neighbor nematic operator $\langle \boldsymbol{q}\rangle_c$. On a flat surface, the average neighbor alignment would simply correspond to the arithmetic mean of the nematic tensors in neighboring cells. However, on a curved surface we need to account not only for in-plane alignment but also for the effect of surface curvature. In particular, since the nematic in each neighboring cell, $\boldsymbol{q}_{c'}$, is constrained to the tangent plane of that cell, we first determine the projection $\boldsymbol{P}_c(\boldsymbol{q}_{c'})$ to the tangent plane of cell c (Fig. S8C), and then determine $\langle \boldsymbol{q}\rangle_c = \sum_{c'} \boldsymbol{P}_c(\boldsymbol{q}_{c'})/n_c$, where n_c is the number of neighboring cells. The dynamics of neighbor alignment is characterized by a time-scale τ_q. We consider a nematic field with a fixed magnitude, describing the average orientation of actin fibers in each cell. The nematic magnitude is maintained equal to 1 through a Lagrange multiplier $m(\boldsymbol{q}_c)$.

To describe the alignment of the nematic field to the local morphogen gradient we first have to calculate the gradient on the curved surface. As mentioned above, we assume that the intra-cellular diffusion is fast compared to inter-cellular diffusion. To estimate the overall morphogen gradient across a cell we have to take into account the morphogen concentrations in neighboring cells (Fig. S8D). For each cell we aim to find a gradient vector $\vec{\nabla}\phi_c$ that satisfies relations $\phi_{c'} = \phi_c + \vec{\nabla}\phi_c \cdot (\vec{r}_{c'} - \vec{r}_c)$ for all neighboring cell c'. However, in general these relations cannot all be satisfied with a single vector and, so we define the morphogen gradient to be the vector $\vec{\nabla}\phi_c$ that produces the least-squared error of these relations (see Supplementary Information for technical details). Finally, due to the nematic symmetry, the nematic will align only to the axis of the morphogen gradient, independent of the polarity of the gradient along this axis. For this reason, the nematic aligns to a tensor constructed as the traceless-symmetric component of the outer product $\vec{\nabla}\phi_c \otimes \vec{\nabla}\phi_c$. The parameter α characterizes the strength of alignment of the nematic to the morphogen gradient.

The choice for all the model parameter values used in the simulations is given in Table S1, and the rationale behind these choices is presented in the SI.

ACKNOWLEDGEMENTS

We thank Erez Braun for many valuable discussions and comments on the manuscript. We thank Gidi Ben-Yoseph for excellent technical help and Lital Shani-Zerbib for her contributions to the development of the image analysis pipeline. We thank Alexandra Schauer, Jana Fuhrmann, Alex Mogilner, Aurelien Roux and Ram Adar for their comments on the manuscript. We thank Ben Atkinson from Intelligent Imaging Innovations for his help in designing the up-and-under spinning disk microscopy system, Nitzan Dahan from the LS&E Imaging Center for advice and help in imaging, Eran Kafri for help in 3D visualization, and the participants of the UCSB 2023 QBio course and the KITP program for discussions and providing a stimulating environment. This

work was supported by a grant from the European Research Council (ERC-2018-COG grant 819174) to KK.

KK dedicates this work to the memory of Naomi Lindenstrauss.

References

Agam, O. and Braun, E. (2023). Universal Calcium fluctuations in Hydra morphogenesis. *Physical biology* **20**, 066002.

Aigouy, B., Cortes, C., Liu, S. and Prud'Homme, B. (2020). EPySeg: a coding-free solution for automated segmentation of epithelia using deep learning. *Development* **147**, dev194589.

Alt, S., Ganguly, P. and Salbreux, G. (2017). Vertex models: from cell mechanics to tissue morphogenesis. *Philosophical Transactions of the Royal Society B: Biological Sciences* **372**, 20150520.

Aufschnaiter, R., Wedlich-Soldner, R., Zhang, X. and Hobmayer, B. (2017). Apical and basal epitheliomuscular F-actin dynamics during Hydra bud evagination. *Biology open* **6**, 1137-1148.

Azzolin, L., Panciera, T., Soligo, S., Enzo, E., Bicciato, S., Dupont, S., Bresolin, S., Frasson, C., Basso, G. and Guzzardo, V. (2014). YAP/TAZ incorporation in the $^{2-}$-catenin destruction complex orchestrates the Wnt response. *Cell* **158**, 157-170.

Blanchard, G. B., Kabla, A. J., Schultz, N. L., Butler, L. C., Sanson, B., Gorfinkiel, N., Mahadevan, L. and Adams, R. J. (2009). Tissue tectonics: morphogenetic strain rates, cell shape change and intercalation. *Nature methods* **6**, 458-464.

Bode, H. R. (2012). The head organizer in Hydra. *Int. J. Dev. Biol.* **56**, 473-478.

Bode, P. M. and Bode, H. R. (1984). Formation of pattern in regenerating tissue pieces of Hydra attenuata: III. The shaping of the body column. *Developmental biology* **106**, 315-325.

Bonfanti, A., Duque, J., Kabla, A. and Charras, G. (2022). Fracture in living tissues. *Trends in Cell Biology*.

Braun, E. and Keren, K. (2018). Hydra Regeneration: Closing the Loop with Mechanical Processes in Morphogenesis. *BioEssays* **40**, 1700204.

Braun, E. and Ori, H. (2019). Electric-induced reversal of morphogenesis in Hydra. *Biophysical journal* **117**, 1514-1523.

Broun, M., Gee, L., Reinhardt, B. and Bode, H. R. (2005). Formation of the head organizer in hydra involves the canonical Wnt pathway. *Development* **132**, 2907-2916.

Broun, M., Salvenmoser, W., Dana, C., Sudol, M., Steele, R., Hobmayer, B. and McNeill, H. (2022). The Hippo pathway regulates axis formation and morphogenesis in Hydra. *PNAS* **119**, e2203257119.

Browne, E. N. (1909). The production of new hydranths in hydra by the insertion of small grafts. *J Exp Zool* **7**, 1-24.

Campbell, R. D., Josephson, R. K., Schwab, W. E. and Rushforth, N. B. (1976). Excitability of nerve-free hydra. *Nature* **262**, 388-390.

Carter, J. A., Hyland, C., Steele, R. E. and Collins, E.-M. S. (2016). Dynamics of mouth opening in Hydra. *Biophysical journal* **110**, 1191-1201.

Cazet, J. F., Cho, A. and Juliano, C. E. (2021). Generic injuries are sufficient to induce ectopic Wnt organizers in Hydra. *Elife* **10**, e60562.

Collinet, C. and Lecuit, T. (2021). Programmed and self-organized flow of information during morphogenesis. *Nature Reviews Molecular Cell Biology* **22**, 245-265.

Comelles, J., Ss, S., Lu, L., Le Maout, E., Anvitha, S., Salbreux, G., Julicher, F., Inamdar, M. M. and Riveline, D. (2021). Epithelial colonies in vitro elongate through collective effects. *Elife* **10**, e57730.

Dye, N. A., Popovic, M., Iyer, K. V., Fuhrmann, J. F., Piscitello-Gomez, R., Eaton, S. and Julicher, F. (2021). Self-organized patterning of cell morphology via mechanosensitive feedback. *Elife* **10**, e57964.

Etournay, R. e., Popovic, M., Merkel, M., Nandi, A., Blasse, C., Aigouy, B. i., Brandl, H., Myers, G., Salbreux, G. and Julicher, F. (2015). Interplay of cell dynamics and epithelial tension during morphogenesis of the Drosophila pupal wing. *Elife* **4**, e07090.
Etournay, R. l., Merkel, M., Popovic, M., Brandl, H., Dye, N. A., Aigouy, B. t., Salbreux, G., Eaton, S. and Julicher, F. (2016). TissueMiner: A multiscale analysis toolkit to quantify how cellular processes create tissue dynamics. *Elife* **5**, e14334.
Farhadifar, R., Roper, J.-C., Aigouy, B., Eaton, S. and Julicher, F. (2007). The influence of cell mechanics, cell-cell interactions, and proliferation on epithelial packing. *Current Biology* **17**, 2095-2104.
Ferenc, J., Papasaikas, P., Ferralli, J., Nakamura, Y., Smallwood, S. and Tsiairis, C. D. (2021). Mechanical oscillations orchestrate axial patterning through Wnt activation in Hydra. *Science advances* **7**, eabj6897.
Fletcher, A. G., Osborne, J. M., Maini, P. K. and Gavaghan, D. J. (2013). Implementing vertex dynamics models of cell populations in biology within a consistent computational framework. *Progress in biophysics and molecular biology* **113**, 299-326.
Futterer, C., Colombo, C., Julicher, F. and Ott, A. (2003). Morphogenetic oscillations during symmetry breaking of regenerating Hydra vulgaris cells. *EPL* **64**, 137.
Gierer, A. (2012). The Hydra model - a model for what? *Int. J. Dev. Biol.* **56:** , 437-445.
Gufler, S., Artes, B., Bielen, H., Krainer, I., Eder, M. K., Falschlunger, J., Bollmann, A., Ostermann, T., Valovka, T., Hartl, M. et al. (2018). beta-Catenin acts in a position-independent regeneration response in the simple eumetazoan Hydra. *Developmental biology* **433**, 310-323.
Guirao, B., Rigaud, S. e. U., Bosveld, F., Bailles, A. i., Lopez-Gay, J. u., Ishihara, S., Sugimura, K., Graner, F. c. and Bellaiche, Y. (2015). Unified quantitative characterization of epithelial tissue development. *Elife* **4**, e08519.
Hannezo, E. and Heisenberg, C.-P. (2019). Mechanochemical feedback loops in development and disease. *Cell* **178**, 12-25.
Hashimoto, H., Robin, F. B., Sherrard, K. M. and Munro, E. M. (2015). Sequential contraction and exchange of apical junctions drives zippering and neural tube closure in a simple chordate. *Developmental cell* **32**, 241-255.
Hobmayer, B., Rentzsch, F., Kuhn, K., Happel, C. M., von Laue, C. C., Snyder, P., Rothbacher, U. and Holstein, T. W. (2000). WNT signalling molecules act in axis formation in the diploblastic metazoan Hydra. *Nature* **407**, 186-189.
Holstein, T. W. (2022). The role of cnidarian developmental biology in unraveling axis formation and Wnt signaling. *Developmental biology*.
Honda, H. and Eguchi, G. (1980). How much does the cell boundary contract in a monolayered cell sheet? *Journal of theoretical biology* **84**, 575-588.
Javois, L. C., Bode, P. M. and Bode, H. R. (1988). Patterning of the head in hydra as visualized by a monoclonal antibody: II. The initiation and localization of head structures in regenerating pieces of tissue. *Developmental biology* **129**, 390-399.
Kier, W. M. (2012). The diversity of hydrostatic skeletons. *Journal of Experimental Biology* **215**, 1247-1257.
Kucken, M., Soriano, J., Pullarkat, P. A., Ott, A. and Nicola, E. M. (2008). An osmoregulatory basis for shape oscillations in regenerating Hydra. *Biophys J* **95**, 978-985.
Latorre, E., Kale, S., Casares, L., Gomez-Gonzalez, M., Uroz, M., Valon, L. e., Nair, R. V., Garreta, E., Montserrat, N., Del Campo, A. a. et al. (2018). Active superelasticity in three-dimensional epithelia of controlled shape. *Nature* **563**, 203-208.

Livshits, A., Shani-Zerbib, L., Maroudas-Sacks, Y., Braun, E. and Keren, K. (2017). Structural inheritance of the actin cytoskeletal organization determines the body axis in regenerating hydra. *Cell Reports* **18**, 1410-1421.
Macklin, M. and Josephson, R. K. (1971). The ionic requirements of transepithelial potentials in Hydra. *The Biological Bulletin* **141**, 299-318.
Maroudas-Sacks, Y., Garion, L., Senthilkumar, S., Popovic, M. and Keren, K. (2024). Confinement modulates axial patterning in regenerating Hydra. *bioRxiv*.
Maroudas-Sacks, Y., Garion, L., Shani-Zerbib, L., Livshits, A., Braun, E. and Keren, K. (2021). Topological defects in the nematic order of actin fibers as organization centers of Hydra morphogenesis. *Nature Physics* **17**, 251-259.
Maroudas-Sacks, Y. and Keren, K. (2021). Mechanical Patterning in Animal Morphogenesis. *Annual Review of Cell and Developmental Biology* **37**, 469-493.
Martino, F., Perestrelo, A. R., Vinarský, V., Pagliari, S. and Forte, G. (2018). Cellular mechanotransduction: from tension to function. *Frontiers in physiology* **9**, 824.
Meinhardt, H. (2012a). Modeling pattern formation in hydra: a route to understanding essential steps in development. *Int. J. Dev. Biol.* **56**, 447-462.
Meinhardt, H. (2012b). Turing's theory of morphogenesis of 1952 and the subsequent discovery of the crucial role of local self-enhancement and long-range inhibition. *Interface Focus* **2**, 407-416.
Merkel, M., Etournay, R. e., Popović, M., Salbreux, G., Eaton, S. and Jülicher, F. (2017). Triangles bridge the scales: Quantifying cellular contributions to tissue deformation. *Physical Review E* **95**, 032401.
Nakamura, Y., Tsiairis, C. D., Ozbek, S. and Holstein, T. W. (2011). Autoregulatory and repressive inputs localize Hydra Wnt3 to the head organizer. *PNAS* **108**, 9137-9142.
Panciera, T., Azzolin, L., Cordenonsi, M. and Piccolo, S. (2017). Mechanobiology of YAP and TAZ in physiology and disease. *Nature Reviews Molecular Cell Biology* **18**, 758-770.
Perros, T., Biquet-Bisquert, A. i., Ben Meriem, Z., Delarue, M., Joseph, P., Marcq, P. and Cochet-Escartin, O. (2023). Mechanical characterization of regenerating Hydra tissue spheres Mechanics of regenerating Hydra. *bioRxiv*, 2023.10. 16.562504.
Petridou, N. I., Spiro, Z. and Heisenberg, C.-P. (2017). Multiscale force sensing in development. *Nature cell biology* **19**, 581-588.
Priya, R., Allanki, S., Gentile, A., Mansingh, S., Uribe, V., Maischein, H.-M. and Stainier, D. Y. R. (2020). Tension heterogeneity directs form and fate to pattern the myocardial wall. *Nature* **588**, 130-134.
Shani-Zerbib, L., Garion, L., Maroudas-Sacks, Y., Braun, E. and Keren, K. (2022). Canalized Morphogenesis Driven by Inherited Tissue Asymmetries in Hydra Regeneration. *Genes* **13**, 360.
Shimizu, H. (2012). Transplantation analysis of developmental mechanisms in Hydra. *Int. J. Dev. Biol.* **56**, 463-472.
Shin, H., Bowick, M. J. and Xing, X. (2008). Topological defects in spherical nematics. *Physical Review Letters* **101**, 037802.
Sinigaglia, C., Peron, S., Eichelbrenner, J., Chevalier, S., Steger, J., Barreau, C., Houliston, E. and Leclère, L. (2020). Pattern regulation in a regenerating jellyfish. *Elife* **9**, e54868.
Soriano, J., Rudiger, S., Pullarkat, P. and Ott, A. (2009). Mechanogenetic coupling of Hydra symmetry breaking and driven Turing instability model. *Biophys J* **96**, 1649-1660.
Stamatakou, E., Hoyos-Flight, M. and Salinas, P. C. (2015). Wnt signalling promotes actin dynamics during axon remodelling through the actin-binding protein Eps8. *PloS one* **10**, e0134976.

Stokkermans, A., Chakrabarti, A., Subramanian, K., Wang, L., Yin, S., Moghe, P., Steenbergen, P., Monke, G., Hiiragi, T., Prevedel, R. et al. (2022). Muscular hydraulics drive larva-polyp morphogenesis. *Current Biology* **32**, 4707-4718. e8.
Suzuki, R., Hiraiwa, T., Tursch, A., Hoger, S., Hayashi, K., Ozbek, S., Holstein, T. W. and Tanaka, M. (2023). Spatio-temporal Coordination of Active Deformation Forces and Wnt/Hippo-Yap Signaling in Hydra Regeneration. *bioRxiv*, 2023.09. 18.558226.
Szymanski, J. R. and Yuste, R. (2019). Mapping the whole-body muscle activity of Hydra vulgaris. *Current Biology* **29**, 1807-1817. e3.
Technau, U., von Laue, C. C., Rentzsch, F., Luft, S., Hobmayer, B., Bode, H. R. and Holstein, T. W. (2000). Parameters of self-organization in Hydra aggregates. *PNAS* **97**, 12127–12131.
Trinh, D.-C., Alonso-Serra, J., Asaoka, M., Colin, L., Cortes, M., Malivert, A., Takatani, S., Zhao, F., Traas, J., Trehin, C. et al. (2021). How mechanical forces shape plant organs. *Current Biology* **31**, R143-R159.
Tursch, A., Bartsch, N., Mercker, M., Schlüter, J., Lommel, M., Marciniak-Czochra, A., Ozbek, S. and Holstein, T. W. (2022). Injury-induced MAPK activation triggers body axis formation in Hydra by default Wnt signaling. *PNAS* **119**, e2204122119.
Vogg, M. C., Beccari, L., Iglesias Ollé, L., Rampon, C., Vriz, S., Perruchoud, C., Wenger, Y. and Galliot, B. (2019). An evolutionarily-conserved Wnt3/²⁻-catenin/Sp5 feedback loop restricts head organizer activity in Hydra. *Nature communications* **10**, 312.
Wang, H., Swore, J., Sharma, S., Szymanski, J. R., Yuste, R., Daniel, T. L., Regnier, M., Bosma, M. M. and Fairhall, A. L. (2023a). A complete biomechanical model of Hydra contractile behaviors, from neural drive to muscle to movement. *PNAS* **120**, e2210439120.
Wang, R., Bialas, A. L., Goel, T. and Collins, E.-M. S. (2023b). Mechano-Chemical Coupling in Hydra Regeneration and Patterning. *Integrative and Comparative Biology* **63**, 1422-1441.
Wang, R., Goel, T., Khazoyan, K., Sabry, Z., Quan, H. J., Diamond, P. H. and Collins, E.-M. S. (2019). Mouth Function Determines the Shape Oscillation Pattern in Regenerating Hydra Tissue Spheres. *Biophys J* **117**, 1145-1155.
Wang, R., Steele, R. and Collins, E.-M. (2020). Wnt signaling determines body axis polarity in regenerating Hydra tissue. *Developmental biology* **467**, 88-94.
Wang, Z., Marchetti, M. C. and Brauns, F. (2023c). Patterning of morphogenetic anisotropy fields. *PNAS* **120**, e2220167120.